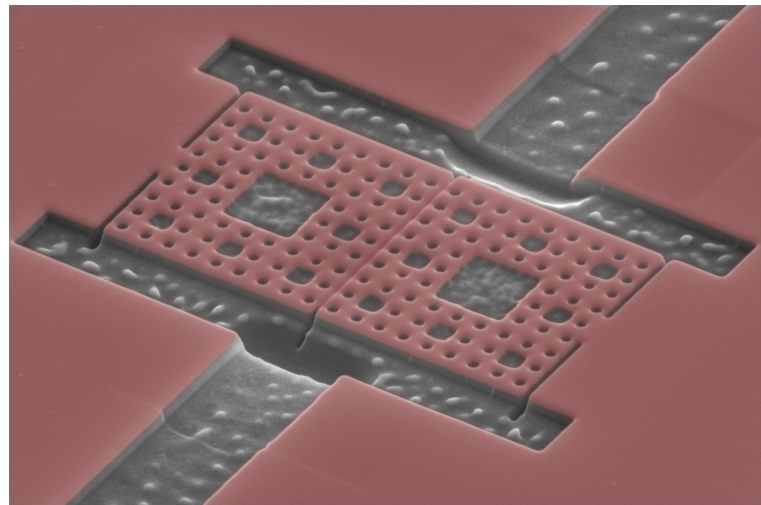




Superconductivity in fractal geometries



THESIS
submitted in partial fulfillment of the
requirements for the degree of
BACHELOR OF SCIENCE
in
PHYSICS

Author: M. Wanrooij
Student ID: 2880199
Principal supervisor : dr. K. Lahabi
Daily supervisor : dr. R. Fermin
2nd corrector : dr. W. Löffler

Leiden, The Netherlands, July 2, 2023

Superconductivity in fractal geometries

M. Wanrooij

Huygens-Kamerlingh Onnes Laboratory, Leiden University
P.O. Box 9500, 2300 RA Leiden, The Netherlands

July 2, 2023

Abstract

Superconductivity is a macroscopic quantum phenomenon based on a transition from a fermionic electron system to a bosonic condensate of electron pairs. This condensate is characterized by two length scales, λ and ξ , which separate superconductivity in a 3D limit (physical system size larger than intrinsic length scales) from lower dimensional structures. Although superconductivity is well studied in both the 3D and 2D limits, little is known about ‘fractional dimensional’ systems, exhibiting a non-integer dimensionality induced by the geometry. This thesis explores the behaviour of planar Josephson junctions featuring electrodes structured as Sierpiński carpet fractals (Hausdorff dimension ~ 1.8). Although the magnetic response of these junctions is dominated by flux-trapping effects, the underlying interference pattern is unconventional and cannot be described by simulations based on the electrode geometry. This warrants further study of the flow of supercurrents in fractional dimensional superconducting systems.

Contents

1	Introduction	1
2	Theory of superconductivity and dimensionality	3
2.1	Superconductivity	3
2.2	Ginzburg-Landau theory	6
2.3	Thin-film limit of the Ginzburg-Landau model and dimensional crossover effects	9
2.4	Probing fractional dimensions	11
3	Simulating fractal-shaped Josephson junctions	17
3.1	Josephson junctions and critical current distributions	17
3.2	Simulating γ over thin-film geometries	20
3.3	Comparing geometries	20
4	Experimental methods	27
4.1	Nanofabrication procedure	27
4.1.1	Electron-beam lithography	27
4.1.2	Sputtering	28
4.1.3	Focused ion beam	31
4.2	Measurement procedure	31
5	Measuring Sierpiński carpet Josephson junctions	33
5.1	FIB results	34
5.2	Resistance versus temperature	37
5.3	Rectangular junction	39
5.4	Fractal junction	41
5.4.1	Vortex trapping effects	41

5.4.2	Isolating the contribution of geometry	44
6	Conclusion and outlook	47
A	Junction physics: some derivations	51
A.1	Derivation of (3.2)	51
A.1.1	Note on macroscopic junctions	55
A.2	Brief note on modifying the formalism to allow non-identical electrodes	56
B	Mathematical background of the Hausdorff and box dimension	57

Introduction

Superconductivity is an active topic of research because of its many applications, ranging from digital circuits to magnetic resonance imaging. In a superconductor, (fermionic) electrons pair up to form Cooper pairs, which are bosonic in nature and as such do not abide by the Pauli exclusion principle. The result is a bosonic condensate that is described by a single wavefunction: a macroscopic quantum system. Superconductors in a magnetic field are characterized by the intrusion of vortices of supercurrent surrounding a core of normal (non-superconducting) metal. Vortex formation and dynamics are governed by two characteristic length-scales, the penetration depth of the magnetic field λ and the coherence length (or vortex radius) ξ , which makes superconductivity sensitive to geometrical considerations. This is especially the case since λ is known to vary strongly depending on film thickness and shape, which can lead to surprising differences between superconducting systems in the 2D (thin-film) and 3D limits. The distribution of supercurrents inside the weak link of a Josephson junction, for example, is known to change significantly when junction dimensions are pushed close to or inside the thin-film limit, where the thickness of the junction becomes comparable to λ and ξ .

Motivated by recent advances in the exploration of fractal geometries in electronic quantum systems [1], we are encouraged to probe the physics of superconducting systems in non-integer dimensions. To this end, we turn again to Josephson junctions: when two superconducting electrodes are separated by a microscopic barrier of non-superconducting material in the presence of a magnetic field, the resulting junction permits transport of supercurrents through the weak link. Various studies have found that the critical current distribution $I_c(B)$ in thin-film planar junctions is determined completely by the sample geometry. Recent advances by [2, 3] show that additional geometry-independent limits on the interfer-

ence pattern of the critical current arise in the case of thin film planar Josephson junctions with finite lateral dimensions.

Having observed new physical behaviour by constraining junctions in three spatial directions, naturally qualifies Josephson junctions as a suitable testing ground for exploring geometries with non-integer (fractal) dimension. Although the influence of dimensionality and dimensional crossover on superconducting systems has been given both theoretical and experimental consideration in literature, the direct implications of using fractal geometries to build Josephson junctions has not been an active field of research. This thesis aims to bridge that gap by probing the critical current distribution for Josephson junctions with fractal electrodes made to resemble Sierpiński carpets, with approximate Hausdorff dimension 1.8928.

The thesis is structured in the following manner. Chapter 2 provides essential theory underlying superconductivity and Josephson junctions. Two fundamental properties of superconducting systems are introduced: the zero resistivity state and the expulsion of applied magnetic fields (the Meissner-effect). Attention is drawn to various models describing superconductivity, in particular the theory of Ginzburg and Landau. The origins and implications of two characteristic length scales, the penetration depth and coherence length, are discussed and explained in the framework of Ginzburg-Landau theory. The coupling of Ginzburg-Landau theory and the Maxwell equations in the thin-film limit is explored, and effects of dimensionality and dimensional crossover on superconductivity are mentioned. We conclude the chapter with a brief discussion of fractal geometries.

In Chapter 3, an approach to simulating the phase distribution over the electrodes of a weakly-coupled, thin-film planar Josephson junction is treated, which is assumed to be symmetric in the y -axis. It is found that the phase distribution can be extracted by solving the Laplace equation over the electrode geometry with appropriate boundary conditions, thus allowing computation of the critical current distribution. This chapter also discusses simulations obtained with COMSOL Multiphysics®. Results motivate the hypothesis that thin-film planar Josephson junctions with fractal electrodes behave qualitatively similar to ordinary thin-film planar junctions in the asymptotic limits of small and large length to width ratios.

Chapter 4 summarizes the various steps in the fabrication of Josephson junctions with fractal electrodes. Experimental results are discussed in Chapter 5 and are related to theory and simulations. Chapter 6 concludes the study and provides recommendations for future research.

Chapter 2

Theory of superconductivity and dimensionality

This chapter discusses fundamental aspects of superconductivity with emphasis on Ginzburg-Landau theory, the thin-film limit and dimensional crossover effects. In addition, some defining properties of fractal geometries are introduced. The reader who is familiar with basic properties of superconducting systems and Ginzburg-Landau theory may consider skipping to Section 2.3 straightforwardly. Most information in this chapter draws from [4], [5] and [6].

2.1 Superconductivity

The theoretical framework surrounding superconductivity is extensive. Roughly speaking, three major theories are recognized. In chronological order, these are the London theory, Ginzburg-Landau (GL) and BCS.* While the London and Ginzburg-Landau models can be seen as phenomenological, the BCS-model, which also formalizes the notion of Cooper pairs that we mentioned in the introduction, is microscopic in nature. In fact, it is possible to retrieve GL from BCS in a suitable limit (in turn, it is possible to derive London theory from GL). To develop our background of Josephson junctions, GL-theory is used. The great advantage of GL is its relative simplicity compared to BCS. We also introduce the London equations to elucidate concepts in GL. BCS will be invoked to make some qualitative statements and underlies the theory of penetration depth in thin films discussed in Section 2.3.

*BCS provides the most comprehensive description of superconductivity up to date and has been granted the 1972 Nobel prize for physics. It is an abbreviation for Bardeen-Cooper-Schrieffer, after J. Bardeen, L. Cooper and J. R. Schrieffer who proposed it in 1957.

Superconductors display a couple of remarkable properties. First off, they exhibit zero resistivity below a critical temperature T_c . Alternatively, this can be framed in terms of the absence of an electric field inside the superconductor (since the general expression for resistivity is $\rho = E/J$, with E the magnitude of the internal magnetic field and J the magnitude of the current density). The underlying reason for the zero resistivity state is complex but surfaces in both the Ginzburg-Landau and the BCS-theory of superconductivity. A concise but incomplete explanation is that the supercurrent represents the collective motion of all Cooper pairs, and is therefore insensitive to small-scale physics such as scattering.

Another fundamental manifestation of superconductivity occurs through the expulsion of applied magnetic fields from the interior of the superconducting material. This phenomenon goes by the name of the Meissner-effect (also known as the Meissner-Ochsenfeld effect). The reason for Meissner expulsion lies in the generation of circulatory supercurrents that oppose the applied magnetic field near the surface of the superconductor (a ‘magnetic mirror’). These currents are referred to as screening currents or Meissner currents and are related to the applied magnetic field through Ampère’s law. The fact that the Meissner effect exists underlines the necessity of explaining superconductivity in a broader scope than the simple idealization of perfect conductivity from classical physics. It might therefore arguably be identified as the most fundamental property of superconductivity.

Figure 2.1 shows the H-T phase diagram for both type-I and type-II superconductors. In type-I superconductors, the Meissner effect results in perfect diamagnetism up to a critical field H_c , above which superconductivity breaks down and the system reverts to the normal state. In type-II superconductors, a mixed state separates the region of perfect diamagnetism from the normal state. Two critical field values exist, H_{c1} and H_{c2} . The mixed state is characterized by the gradual penetration of magnetic flux through quantized flux vortices, each carrying a flux $\Phi_0 = h/2e$ (approximately 2.0678×10^{-15} Wb). The distribution and dynamics of vortices over the geometry of a superconductor is a rich topic on its own that is governed by arguments of symmetry. The most compact configuration of vortices is a hexagonal lattice arrangement, called the Abrikosov lattice.[†]

[†]In reality the categorization of superconductors in type I and type II is supplemented with type-1.5 superconductors. In addition, an intermediate-mixed state may be reached in some geometries. An introductory treatment can be found in [7].

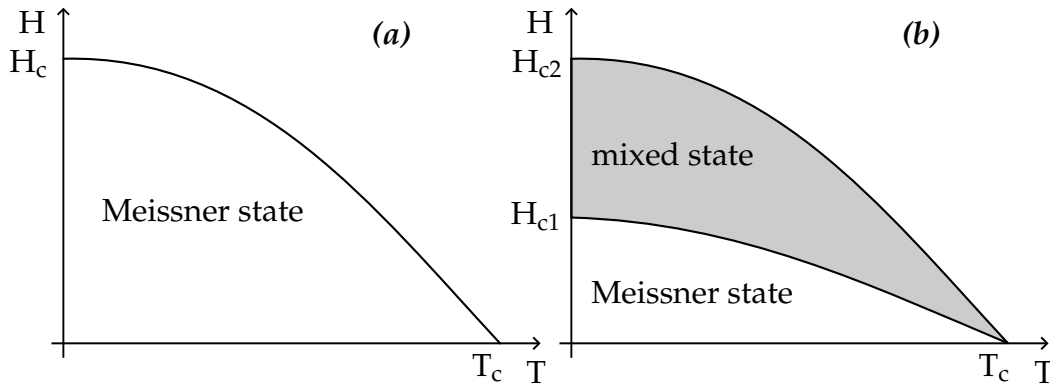


Figure 2.1: H - T phase diagrams indicating critical field boundaries. (a) H - T for a type-I superconductor, with only the Meissner state. (b) In a type-II superconductor, a mixed state exists that features the intrusion of vortices into the geometry.

A simple description that captures the relation between the superconducting current distribution \mathbf{J}_s and the electromagnetic fields \mathbf{E} and \mathbf{B} within the superconductor is given by the London equations:

$$\frac{\partial \mathbf{J}_s}{\partial t} = \frac{n_s e^2}{m} \mathbf{E} \quad (2.1)$$

$$\nabla \times \mathbf{J}_s = -\frac{n_s e^2}{m} \mathbf{B} \quad (2.2)$$

where n_s is the superconducting carrier density. The Meissner effect can be distilled from the second London equation by applying Ampère's law to equation (2.2) and invoking a vector calculus identity. In terms of the parameter λ_L , assembled from μ_0 (originating from Ampère's law) and the constants in equation (2.2) as $\lambda_L = \sqrt{\frac{m}{4\mu_0 n_s e^2}}$, it reads:

$$\nabla^2 \mathbf{B} = \frac{1}{\lambda_L^2} \mathbf{B} \quad (2.3)$$

This equation permits exponentially decaying solutions with decay constant λ_L , which is called the London penetration depth.

$$B_z(x, y, z) = B e^{-\frac{x}{\lambda_L}} \quad (2.4)$$

In essence, λ_L represents the characteristic distance for suppression of the magnetic field inside the superconductor, close to the interface between the superconducting material and the exterior [8]. While the magnetic field decreases inwardly (measured from the surface of the superconductor), the screening currents are subjected

to the same exponential decay:

$$J_y(x, y, z) = \frac{B}{\mu_0 \lambda_L} e^{-\frac{x}{\lambda_L}} \quad (2.5)$$

Although the London equations do not have a ‘rigorous’ derivation, they can be justified by a simple argument based on the Drude model when letting the characteristic scattering time $\tau \rightarrow \infty$. Alternatively, a quantum mechanical motivation based on canonical momentum is possible; see [5, p. 4-6]. Pippard realized however that changes in the superconducting wavefunction are nonlocal, and connected their characteristic spatial scale to a ‘superconducting mean free path’ ξ_0 : quantities such as n_s are sensitive to a region of radius ξ_0 around the point of interest (the coherence length). In the London model it is assumed that the supercurrent density and the flux density vary over typical length scale λ_L . The applicability of the London model does therefore not extend to arbitrary superconducting systems but is adequate only if $\lambda_L > \xi_0$. Superconductors with $\xi_0 \gg \lambda_L$ are called *Pippard superconductors* and obey nonlocal arguments, for which Pippard proposed a non-local generalization of the London equations in analogy to Chambers’s nonlocal generalization of Ohm’s law [5, pp. 6-7, 100-101].

2.2 Ginzburg-Landau theory

Since the theory of superconductivity is a theory of phase transition, it can be characterized by an order parameter.[‡] The order parameter, denoted by ψ in the theory of Ginzburg and Landau, is postulated as an (unspecified) complex-valued physical quantity which differentiates between the disordered state above T_c and the ordered state below T_c by taking on a non-zero value below the critical temperature:

$$\psi = \begin{cases} 0 & T > T_c \\ \psi(T) \neq 0 & T < T_c \end{cases} \quad (2.6)$$

The physical interpretation of ψ becomes clear in the context of (the microscopic) BCS-theory, from which GL can be recovered in a suitable limit (for a more detailed account of the relation between BCS and GL, consult [11] and [12]). Essentially, $|\psi|^2$ represents the density of Cooper pairs in the superconductor as put

[‡]In fact, the exact order of the superconducting phase transition has long been a topic of confusion. The contemporary understanding, supported by theoretical and simulational evidence, identifies the transition as being of first order in the type I regime and of second order in the type II regime with a tricritical point separating these regimes [9, 10].

forth in the BCS-framework.

The distribution of the order parameter within a superconducting material is governed by the first Ginzburg-Landau equation, which can be derived from thermodynamic principles. In the presence of a magnetic field and as a function of radial distance, it is given by:

$$-\frac{\hbar^2}{2m_*} \left(\nabla + \frac{2ei}{\hbar} \mathbf{A} \right)^2 \psi(\mathbf{r}) + (a + b|\psi|^2)\psi(\mathbf{r}) = 0 \quad (2.7)$$

Here, \mathbf{A} is the vector potential for the applied magnetic field, while m_* is a measure for the energy cost associated with gradients in $\psi(\mathbf{r})$ and can be interpreted as the effective mass of the quantum system. a and b (with $b > 0$) represent two phenomenological parameters that are smooth functions of temperature. Despite the apparent similarity of the first Ginzburg-Landau equation to the Schrödinger equation, note the nonlinearity arising from the second term in brackets.

It is stressed again that the order parameter $\psi(\mathbf{r})$ is a complex quantity and is therefore equipped with both amplitude and a (spatially dependent, gauge-covariant) phase, $\gamma(\mathbf{r})$:

$$\psi(\mathbf{r}) = |\psi(\mathbf{r})| e^{i\gamma(\mathbf{r})} \quad (2.8)$$

Taking this into consideration, the superconducting current density can be extracted from equation (2.7) by performing a functional derivative with respect to the free energy, as outlined in [4]:

$$\mathbf{j}_s = -\frac{2e}{\hbar} \rho_s \left(\nabla \gamma + \frac{2e}{\hbar} \mathbf{A} \right) \quad (2.9)$$

Equation (2.9) is called the second Ginzburg-Landau equation. ρ_s is the superfluid stiffness which is directly proportional to the London superfluid density n_s by the relation $\rho_s = n_s \hbar^2 / 4m_e$. After some manipulation, the equation can be written in a more suggestive form:

$$\mathbf{j}_s = -\frac{\Phi_0}{2\pi\mu_0\lambda^2} \left(\frac{2\pi}{\Phi_0} \mathbf{A} + \nabla \gamma \right) \quad (2.10)$$

where we have expressed the constants in terms of the familiar magnetic flux quantum Φ_0 and the penetration depth. It is customary to define $m_e = 1/2m_*$ and $n_s = 2|\psi|^2$. As hinted before, BCS-theory allows us to identify $|\psi|^2$ as the density of Cooper pairs in the ground state; n_s then naturally represents the density of electrons belonging to Cooper pairs. m_* can be interpreted as the mass of a Cooper

pair (which is twice the electron mass m_e). It is remarked that λ is a temperature-dependent quantity. The temperature dependence is specified through:

$$\lambda(T) = \lambda(0) \frac{1}{\sqrt{1 - (T/T_c)^4}} \quad (2.11)$$

The lower and higher critical fields that are sustained by a (type-II) superconductor in a magnetic field normal to the surface are given by [4, p. 89] and [5, p. 119]:

$$H_{c1}(T) = \frac{\Phi_0}{4\pi\mu_0\lambda^2} \ln\left(\frac{\lambda}{\xi}\right) \quad (2.12)$$

$$H_{c2}(T) = \frac{\Phi_0}{2\pi\xi^2(T)} \quad (2.13)$$

where

$$\xi(T) = \frac{\Phi_0}{2\sqrt{2}\pi H_c(T)\lambda_{eff}(T)} \quad (2.14)$$

is the superconducting coherence length, a measure for the spacing between electrons in a Cooper pair, or the characteristic exponent for the phase transition from the superconducting to the normal state. Alternatively, ξ can be viewed as the radius of a vortex, and λ as the typical lengthscale for decay of magnetic field away from the vortex. In eq. (2.14), H_c represents the thermodynamic critical field (the field at which condensation energy balances the energy associated with the counteracting pressure induced by the external magnetic field) and λ_{eff} is an effective penetration depth that corrects for nonlocal effects, such as may arise in the thin-film limit (Section 2.3) or in Pippard superconductors ($\xi_0 \gg \lambda_L$). It is extracted from measurements or computed from the microscopic (BCS) theory.

As a concluding remark on this section, the dimensionless parameter κ is introduced:

$$\kappa = \frac{\lambda}{\xi} \quad (2.15)$$

This quantity is called the Ginzburg-Landau parameter and is used to distinguish type-I from type-II superconductors. Landau proposed that for type-I superconductors $0 < \kappa < 1/\sqrt{2}$, whereas type-II superconductors have $\kappa > 1/\sqrt{2}$. The given values emerge naturally from Abrikosov's analysis of the Ginzburg-Landau equations of bulk superconductors in a magnetic field [4, pp. 83-89]. [13] notes that for $\kappa \rightarrow \infty$, vortices appear as line singularities (vanishing vortex radius) and the Ginzburg-Landau model effectively reduces to the London model.

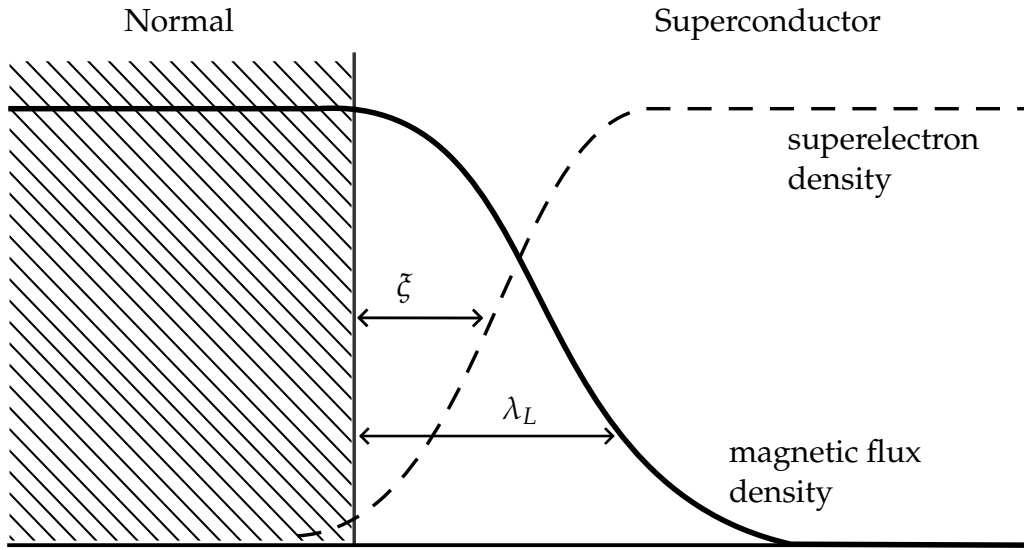


Figure 2.2: Penetration depth λ_L and coherence length ξ on the normal metal-superconductor interface.

2.3 Thin-film limit of the Ginzburg-Landau model and dimensional crossover effects

In the previous section, Ginzburg-Landau theory has been treated in the context of (three-dimensional) bulk superconductivity. In the two-dimensional thin-film limit, as the film thickness d becomes comparable to λ and ξ , nonlocal electrodynamics starts making its mark on superconductivity and we can no longer rely on λ_L , which was derived for bulk superconductors with a local response. Instead, the supercurrent response of a thin-film, nonlocal superconductor relies on modified expressions of λ_L . It turns out that a distinction is necessary based on whether the field is applied in parallel or perpendicular to the film. The parallel case is described succinctly in [5, pp. 104-105] and relies on the BCS range function $J(R, T)$, which is a measure of the ‘degree of nonlocality’ at temperature T and resistance R .

In the perpendicular case, subject to the constraint $d \ll \lambda$, not only is nonlocality a leading consideration, but the situation is further complicated by the influence of geometrical effects on the solutions of the two-dimensional Maxwell equations. [14] showed that the penetration depth becomes thickness-dependent:

$$\lambda_{\perp} \simeq \lambda_L^2 / d \gg \lambda_L \quad (2.16)$$

with $2\lambda_L^2/d$ also called the ‘Pearl length’.

To expand on the underlying mechanism, it is essential to realize that the Ginzburg-Landau equations, which govern the current distribution inside the superconductor, are generally not independent from the Maxwell equations determining the fields outside of the superconducting geometry. Instead, the two sets of equations are coupled through the boundary conditions on the sample. In the case of thin films, coupling is considerably altered compared to the bulk regime. [13] found that for a thin film of thickness d and typical lateral dimension L , the Ginzburg-Landau model can be simplified by expanding variables in a power series based on the aspect ratio $\epsilon = L/d$ while retaining leading order contributions. Three regimes are found for the thin-film limit that are characterized by the parameter $\Lambda = \lambda^2/Ld$:

1. if Λ is order 1 (i.e. the effective screening length and the lateral film dimensions are of the same order), the electric current inside the film and the applied magnetic field are coupled;
2. if $\Lambda \gg 1$, the applied magnetic field passes through the film (to leading order) and the current and field are decoupled;
3. if $\Lambda \ll 1$, the vorticity in the film determines magnetic field, which then determines the current in the film; again, the problem is decoupled.

Effects such as those materializing in thin-film superconductors result from constricting the geometry of the system in one dimension (the ‘thin-film limit’). We saw that the interaction between physical processes is critically influenced by the length scales involved in the problem. The coupling between Ginzburg-Landau theory and the Maxwell equations is not the only mechanism influenced by dimensional crossover. 2D- to 1D-transitions, for example, bring along their own set of peculiarities.

2D to 1D transitions in superconducting systems have been studied extensively in nanowires, where breakdown of the superconducting state occurs when long range phase coherence is lost due to quantum phase slips. Dimensional crossover in nanowires has been reported by various authors, among others [15–17], and is reviewed in some detail by [18]. [19] finds that the superconducting transition in nanowires becomes broader when the diameter of the wires is decreased; the cause is attributed to macroscopic quantum tunnelling of the phase of the order parameter at low temperatures. A gradual crossover to normal or weakly insulat-

ing behaviour is found in long nanowires [20].[§]

2D-1D crossover is also reported in Josephson junction arrays. [21, 22] explores dimensional crossover for planar Josephson junction arrays from the superconducting to the insulating regime in the temperature dependence of resistance and in the IV curves. The change is explained qualitatively in terms of the competition between the Josephson effect and quantum phase fluctuations induced by charging effects, which dominate in lower dimensional arrays. The charging effects are the result of the Coulomb blockade of Cooper pairs in the junctions that develops because the junction (two electrodes separated by a small distance) has a non-negligible capacitance. Measurements in [22] were conducted on arrays of small-capacitance Josephson junctions on a Si-substrate, of which 48 were placed in the direction of the current and a varying number (1, 2, 4, 8, 20 or 40) transverse to the current to imitate the crossover from line to rectangle.

To converge toward the main interest of this thesis, which is the junction response in non-integer dimensions, it was shown by [23] that a crossover between Euclidean and fractal regimes exists in Josephson junctions *arrays*. In this study, distinct behaviour of the sample magnetoinductance $L(f)$ in junction arrays of periodically repeating Sierpiński triangles exposed to a perpendicular magnetic field is found. The crossover between Euclidean and fractal regime depends on the relation between intervortex distance and the size of constituent triangles, and can be expressed in terms of the frustration parameter f , which represents the number of flux quanta penetrating an elementary unit cell of the structure.

It deserves mention that the manifestation of superconductivity is itself limited to certain length scales. A lower limit on the particle size was conjectured by Anderson in 1959 to be of the order of 10^4 - 10^5 electrons [24]. The validity of Anderson's claim is reinforced by experimental results from [25].

2.4 Probing fractional dimensions

Figure 2.3 shows the first four iterations of a Sierpiński carpet. The Sierpiński carpet is an example of a *fractal geometry*, also known as a *fractal*. The defining property of a fractal is its scale-invariancy: fractals are (geometric) objects that

[§]A discussion on the crossover from a disc to a thin ring, as well as information on superconductivity in other micro- and mesoscopic systems with geometries such as lines, triangles and discs, loop clusters, disc clusters, etc., is found in [7].

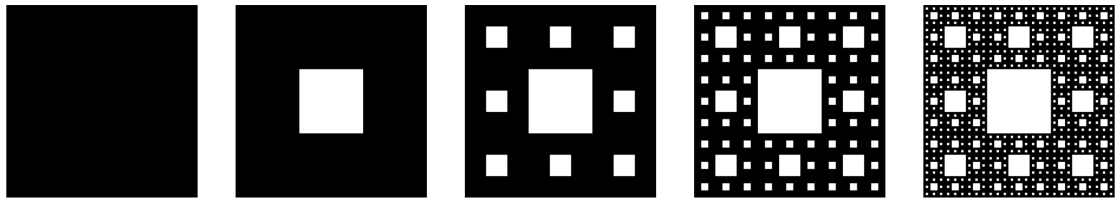


Figure 2.3: The zeroth, first, second, third and fourth iteration of the Sierpiński carpet. In the first iteration, a square is divided into 9 equal subsquares and the middle square is removed. The procedure is repeated recursively on each of the subsquares for subsequent iterations. The Sierpiński carpet has Hausdorff dimension $\log 8 / \log 3 \sim 1.8928$.

are the union of rescaled copies of themselves. Depending on whether the rescaling is isotropic in all directions, we speak about *self-similar* or *self-affine* fractals. The Sierpiński carpet is a self-similar fractal, which implies the isotropic rescaling property. Fractal structure can surface in both spatial and temporal patterns, or – expressed in the most general sense – in any set whose elements demonstrate a self-invariant structure.

Equipping fractal objects with dimensionality has given rise to a mathematical interpretation of the term ‘dimension’ that is richer than the notion of dimensionality applied to standard (non-fractal) Euclidean geometries. Expanded definitions of dimension aim to take this additional complexity, that is grounded in the self-invariant structure of the fractal object, and encode it in the dimension they assign to the geometry. The resulting *fractal* dimension is characterized by non-integer values.

Fractal dimension, just like non-fractal dimension, establishes the relation between the scaling of a set and the amount of detail that appears on the respective scale. For Euclidean geometries, this interpretation can be seen to produce the familiar sense of dimension. Consider for example the scaling of a line. Dividing a line into n equal-sized elements, i.e. scaling the line by $1/n$, it is evident that the original geometry can be reassembled from the n resulting pieces. In this example, the amount of detail, n , is specified by the number of line segments. Its relation to the scaling parameter $1/n$ is fixed through an exponent:

$$n = \left(\frac{1}{n}\right)^{-1} \quad (2.17)$$

We see that the exponent takes on value 1. As such, we assign the line a dimension of 1. In a similar way, a unit square is the union of n^2 rescaled squares of side $1/n$,

corresponding to a scaling exponent of 2. The same procedure applied to a unit cube yields dimension 3, etcetera (Figure 2.4).

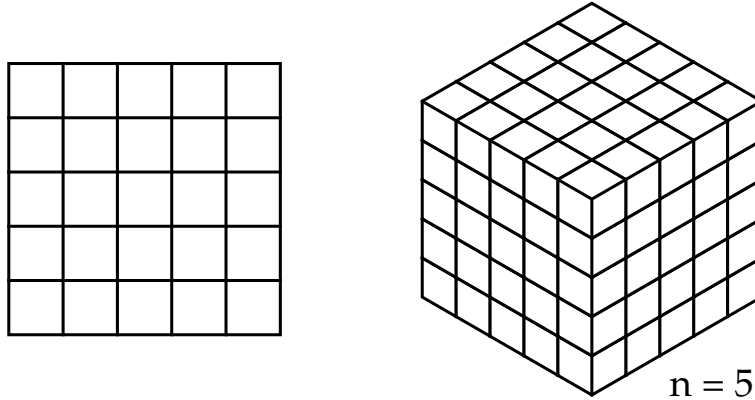


Figure 2.4: A unit square can be subdivided into n^2 squares of side $1/n$, and a unit cube into n^3 cubes of side $1/n$.

For the Sierpiński carpet, however, successive scaling operations cut the sides of the square into three parts and subdivide the pattern into 9 smaller squares. By taking out the middle square, we are left with 8 squares. The corresponding scaling relation is given by:

$$8 = \left(\frac{1}{3}\right)^{-D_f} \quad (2.18)$$

From this we are able to retrieve the value of D_f , the (fractal) dimension of the geometry, as follows:

$$D_f = -\frac{\log 8}{\log 1/3} \sim 1.8928 \quad (2.19)$$

which is non-integer. We can make this approach more general in an informal manner. Let N denote the amount of detail of a geometry and ϵ the scaling parameter. Then the scaling dimension D_f is given by the ratio of logarithms of N and ϵ :

$$D_f = -\frac{\log N}{\log \epsilon} \quad (2.20)$$

From the examples and the description above, there is no way to infer rigorously what ‘detail’ constitutes, and for more complicated fractals, this is not at all self-explanatory. A solution is found in expanding the notion of dimensionality beyond the Euclidean case by defining the Hausdorff dimension. A very brief treatment of

the Hausdorff dimension, as well as its relation to the box counting (Minkowski-Bouligand) dimension, which is the topic of the remainder of this section, is provided in Appendix B.

In most cases, applying eq. (2.20) or, for that matter, the Hausdorff dimension to an arbitrary fractal is highly non-trivial. More often than not, determining fractal dimension via the Hausdorff approach is an exercise reserved to mathematicians.[¶] Instead, in fields that require processing of fractal datasets, it is opted to apply numerical methods. One such approach for determining the fractal dimension of arrays of visualized data is the box counting method, in which the image is overlaid with a grid of boxes and the number of boxes containing relevant details of the data is tallied. The procedure is repeated with grids of varying size, to introduce a scaling dependency. A logarithmic regression line is then fitted to the N vs ϵ -characteristic to retrieve D_f . Figure 2.5 illustrates the principle of box counting applied to the coastline of Great Britain (box counting dimension ~ 1.25). Other methods to evaluate the fractal dimension of spatial patterns are the cluster dimension, the Korcak patchiness exponent and the Hurst exponent [6].

An important (and perhaps encouraging) property of the box counting method is that it should, at least in principle, yield a dimension equivalent to the Hausdorff dimension whenever a fractal fulfils the open set condition (OSC) – which is true for most ‘well-behaved’ fractals. This is the gist of Proposition B.0.1. Of course the limitations imposed on computational systems prevent the estimate from ever really replicating the Hausdorff dimension with infinite precision. However, Proposition B.0.1 states that there stands nothing in the way of infinitely increasing the precision of the estimate, to the extent that the system specifications permit further increments in the resolution.

In addition to resolution, multiple factors influence the quality of the box counting estimation. The grid position for instance controls to some degree the way the image is overlaid with boxes and therefore contributes to the box count. To mitigate orientation bias, sampling can be performed with multiple grid orientations or with sliding scans. Another prominent example is the handling of non-binary data such as grayscale images; this requires a rule for averaging the intensities of pixel values (taking into consideration e.g. the relative importance of foreground and background pixels). Oftentimes, considerations like these boil down to an op-

[¶]To appreciate why deriving D is non-trivial in most instances consider, for example, the rather long and tedious proof delivered by M. Shishikura, on the Hausdorff dimension of the boundary of the Mandelbrot set [26].

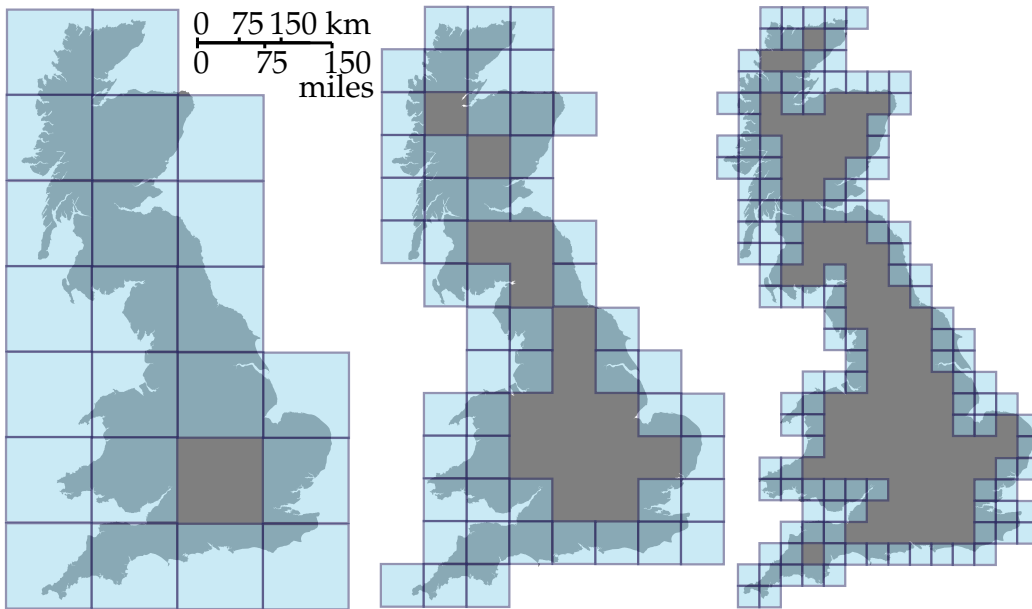


Figure 2.5: Three coverings of a geometry (the coastline of Great Britain), representing sequential steps in estimating its box counting dimension. With decreasing ϵ , the number of boxes $N(\epsilon)$ required to cover the geometry increases. D_f is acquired by fitting a logarithmic regression line to $N(\epsilon)$. Image adapted from [27].

timization problem. Software such as FracLac for imageJ has built-in methods to deal with said complications and can therefore be said to provide a more reliable numerical implementation than most naive approaches to the problem [28, 29].

Simulating fractal-shaped Josephson junctions

We move on to treating the distribution of critical currents in Josephson junctions. A theoretical description is followed by simulations in COMSOL Multiphysics®. The analysis presented in this chapter roughly follows [3]. Most technical details are omitted, but can be found in [3] or in Appendix A.

3.1 Josephson junctions and critical current distributions

As stated in the introduction, Josephson junctions are devices of two or more superconducting electrodes divided by a thin *barrier* or *weak link*. Examples of weak links are insulating barriers (the resulting structure is known as an SIS-junction) and strips of non-superconducting metal (SNS-junction). In the presence of a phase gradient, a Josephson junction permits transport of supercurrent through the weak link even in the absence of a voltage difference, provided that the link is narrow. This is the case if the superconducting order parameters from the left and right electrodes, ψ_L and ψ_R , demonstrate sufficient overlapping in the weak link. The fact that the weak link is narrow allows the superconducting state to persist even though the order parameters degrade (exponentially) over the non-superconducting interlayer.* Figure 3.1 shows a schematic of a Josephson junction.

*This is known as the *proximity effect*.

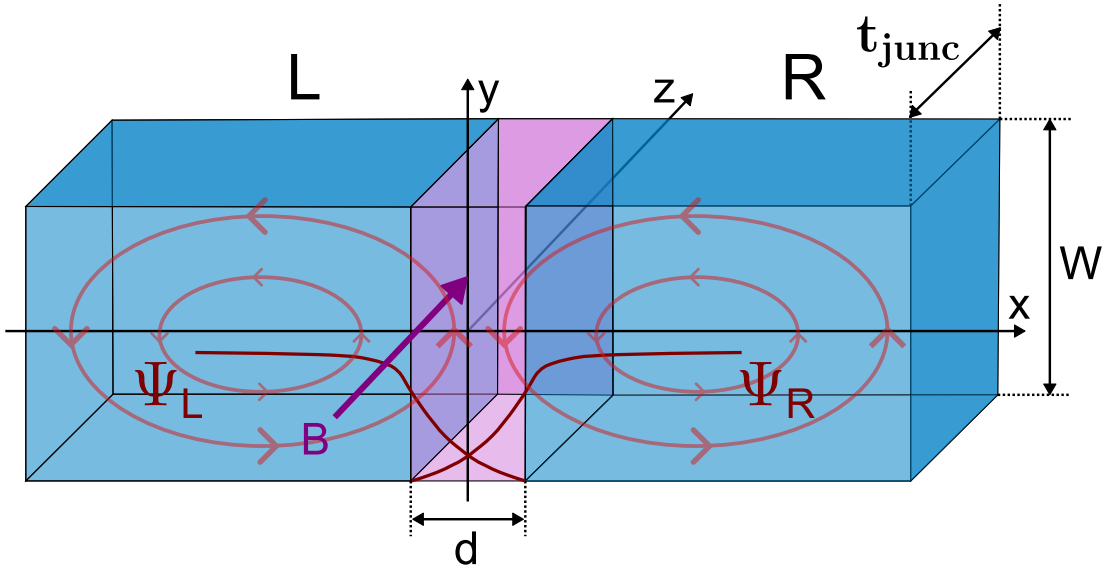


Figure 3.1: Schematic of a Josephson junction of width W and thickness t_{junc} along the x -axis. A left (L) and a right (R) superconducting electrode are separated by a weak link spanning a distance d . The order parameters ψ_L and ψ_R decay exponentially inside the non-superconducting barrier, but their overlap at the centre of the weak link is sufficient to allow a notable supercurrent to flow through the junction. An applied magnetic field $\mathbf{B} = B\hat{\mathbf{z}}$ generates screening currents (red) inside the superconducting electrodes. These screening currents produce an interference pattern inside the weak link. Image adapted from [8].

If the electrodes are weakly coupled – that is, if the current between the electrodes is small – the current-phase relation for a Josephson junction can be expressed as the first harmonic of a trigonometric series [8]:

$$\mathbf{J} = \mathbf{J}_c \sin(\varphi) \quad (3.1)$$

where φ is the phase difference over the junction and \mathbf{J}_c the critical current. This is known as the first Josephson relation.

It has been found that the phase difference $\varphi(y)$ over a weak link of width d oriented along the x -axis (from $x = -d/2$ to $x = +d/2$) follows from the second Ginzburg-Landau equation (eq. (2.9)) under the assumption that the electrodes are symmetric with respect to the y -axis and with the gauge fix $A_y = 0$. Again, weak coupling between the electrodes is assumed, approximated as $J_x(\pm\frac{d}{2}, y) = 0$. The critical current as a function of magnetic field is then obtained by integrating the first Josephson relation eq. (3.1) over the cross-section and current-biasing the

junction by setting $\varphi_0 = \pi/2$. Here, we have assumed a uniform zero-field critical current density over the junction. The resulting expression, simplified for junctions with d small, is:

$$\frac{I_c(B)}{I_c(0)} = \frac{1}{W} \left| \int_{-W/2}^{W/2} \cos \left(2B\gamma \left(\frac{d}{2}, y \right) \right) dy \right| \quad (3.2)$$

A detailed derivation of equation (3.2) is given in Appendix A.

It is emphasized that these results were derived in the limit for thin-film planar Josephson junctions. For macroscopic junctions, the relation changes (see note in Subsection A.1.1) because the phase difference assumes a slightly simpler form. The resulting expression for the critical current as a function of the applied magnetic field then assumes the shape of a classic Fraunhofer interference pattern: a sinc function periodic in Φ . In this light, eq. (3.2) can be seen as an adjusted Fraunhofer pattern. It turns out that for thin-film planar Josephson junctions, the interference pattern is modified such that the peak height decays less strongly than $1/B$, and the side lobes are broader than half the size of the middle lobe [3].

In the derivation of eq. (3.2), we assumed a uniform zero-field distribution of $J_c(y)$. It is nonetheless worth mentioning that the critical current $J_c(y)$ over the junction – if it only has a y -dependence – and $I_c(B)$ are related through the Fourier transform, as proposed by [30]:

$$I_c(B) = \mathcal{F}\{J_c(y)\} = \left| \int_{-\infty}^{\infty} J_c(y) e^{i\varphi_B(B,y)} dy \right| \iff J_c(y) = \mathcal{F}^{-1}\{I_c(B)\} \quad (3.3)$$

For macroscopic junctions with $\varphi_B(y) = 2\pi L_{eff}By/\Phi_0$ (Subsection A.1.1), this is more conveniently expressed when making the change of variables to the reduced field $\beta = L_{eff}B/\Phi_0$ such that y and β are conjugate:

$$I_c(\beta) = \left| \int_{-\infty}^{\infty} J_c(y) e^{2\pi i \beta y} dy \right| \quad (3.4)$$

For junctions in the thin-film limit however, $\varphi_B(y)$ is given by eq. (A.6), which calls for the use of a new set of conjugate variables that is considerably more convoluted; the resulting transform is less straightforward. The technical details are omitted here, but can be found in detail in [3, 8].

3.2 Simulating γ over thin-film geometries

In Section 3.1, a method for deriving the supercurrent distribution over the width of a thin-film planar Josephson junction was discussed. The key question remaining is how to find the distribution of γ over an arbitrary thin-film geometry. Knowing this distribution allows extraction of $\gamma\left(\frac{d}{2}, y\right)$, and consequently computation of $I_c(B)$ with eq. (3.2). Fortunately, [3] provides a methodology to find γ , based on previous work by [2]. Essentially, the procedure maps the second Ginzburg-Landau equation (eq. (2.10)) onto the Laplace equation:

$$\nabla^2 \gamma = 0 \quad (3.5)$$

This is achieved by imposing a physical constraint on the supercurrent while fixing the magnetic vector potential through the Coulomb gauge:

$$\nabla \cdot \mathbf{J} = 0 \quad (3.6)$$

$$\nabla \cdot \mathbf{A} = 0 \quad (3.7)$$

Note that eq. (3.6) is physically equivalent to stating that supercurrent is conserved over the geometry. Equation (3.5) can be solved for γ given appropriate boundary conditions. These arise naturally from the requirement that no supercurrent exits the geometry at the boundaries. We also assume weak coupling between the electrodes ($J_x(\frac{d}{s}, y) = 0$) which effectively imposes the same constraint at the weak link-electrode interface. If $\hat{\mathbf{n}}_R$ denotes the unit vector normal to the boundary (pointing inwards towards the superconductor), then, using eq. (2.10), the aforementioned requirements can be cast into the following set of Neumann boundary conditions:

$$\nabla \gamma \cdot \hat{\mathbf{n}}_R = -\frac{2\pi}{\Phi_0} \mathbf{A} \cdot \hat{\mathbf{n}}_R \quad (3.8)$$

Equation (3.8) can be evaluated individually for all boundaries in the geometry by choosing a suitable parametrization for $\hat{\mathbf{n}}_R$. For a Sierpiński carpet with sides oriented parallel to the x- and y-axis, deriving the unit normal vectors is especially simple since the geometry only consists of straight line segments. For the Sierpiński carpet in Figure 3.2, the unit normal vectors and values of eq. (3.8) are listed in Table 3.1. Here, the gauge fix $A_y = 0$ is made for simplification purposes.

3.3 Comparing geometries

We are now equipped with all the tools to compute the interference pattern of thin-film, planar Josephson junctions with electrodes of arbitrary shape. As a next step,

we wish to compare interference patterns generated by the geometries presented in Figure 3.2. In line with [3], we characterize the interference pattern by the width of the fifth side lobe, which we call ΔB . [3] found that ΔB reaches asymptotic limits for both $L \gg W$ and $L \ll W$ in the case of rectangular, rhomboidal and elliptical electrodes, which were all the geometries considered in the study. Here, W describes the width of the junction, and L the length (refer to Figure 3.2). In terms of the dimensionless aspect ratio A/W^2 , where A denotes the electrode surface area, the asymptotes emerged geometry independent and were (numerically) determined to fit the lines $\Delta B = 2\Phi_0/A$ and $\Delta B = 1.842\Phi_0/W^2$. [3] also found that ΔB follows the general expression:

$$\Delta B = \frac{\pi}{2} \frac{1}{\max\{\gamma/B\}} = \frac{\pi}{2} \frac{B}{\gamma(\frac{d}{2}, \frac{W}{2})} \quad (3.9)$$

which is, again, geometry independent.

To find γ over thin-film geometries, simulations are performed with COMSOL

Table 3.1: Boundary cases of Figure 3.2, corresponding unit normal vectors $\hat{\mathbf{n}}_R$ and the value of eq. (3.8), with gauge fix $A_y = 0$.

Boundary	$\hat{\mathbf{n}}_R$	$\nabla \gamma \cdot \hat{\mathbf{n}}_R$
1	$+\hat{\mathbf{x}}$	$\frac{2\pi B}{\Phi_0} y$
2	$-\hat{\mathbf{x}}$	$-\frac{2\pi B}{\Phi_0} y$
3	$\pm\hat{\mathbf{y}}$	0

Multiphysics® 6.0. COMSOL uses the finite elements method to discretize the geometry and numerically evaluates the Laplace equation subject to the boundary conditions in Table 3.1. The mesh was built using a free triangular grid with dynamic sizing. A maximum element size of $(0.018L/40 + 0.002)*1.5$ was found to provide a good compromise between computational efficiency and precision. The stationary solver operated with a relative tolerance of 0.01.

Our first aim is to build some intuition regarding the interpretation of planar junction interference patterns, both for this chapter and for the upcoming discussion of experimental results. Figure 3.3 presents the simulated interference pattern of a rectangular junction and of a junction with second order Sierpiński carpet electrodes (Figure 3.2). Surprisingly, the patterns are found to exhibit excellent qualitative correspondence, even though the rectangular junction contains neither holes

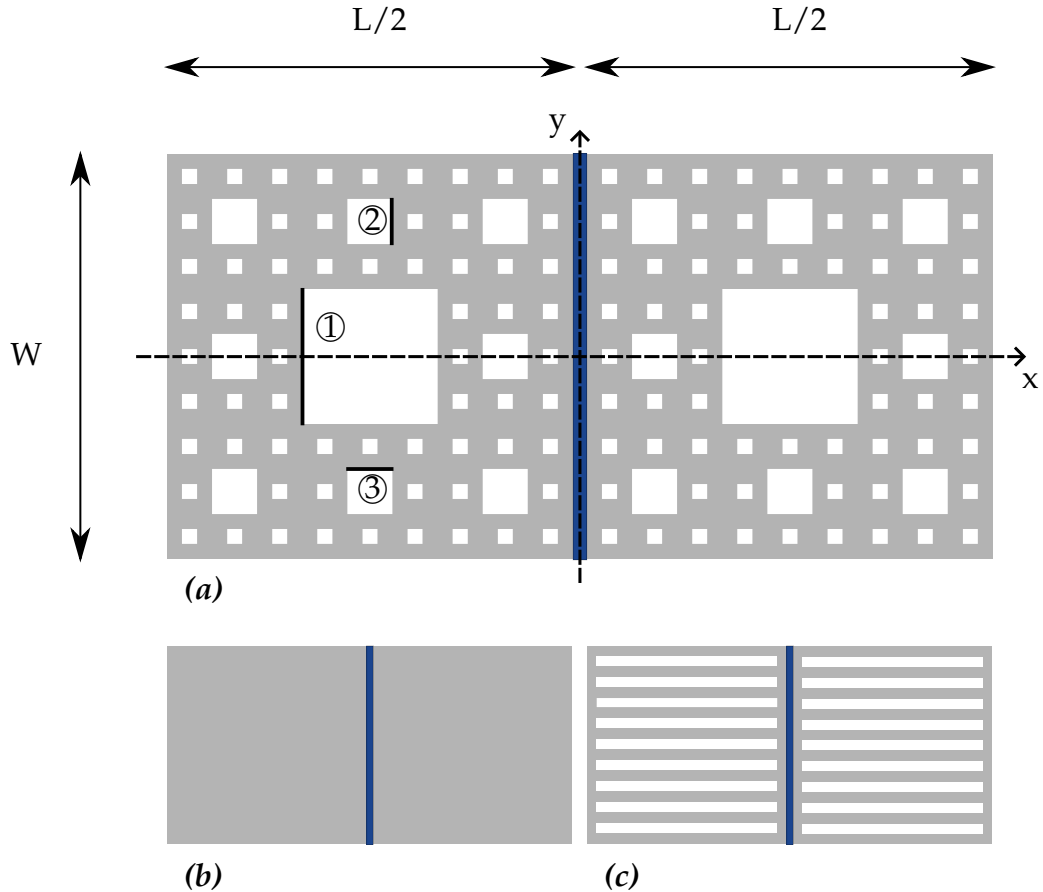


Figure 3.2: (a) Schematic of a thin-film planar Josephson junction of width W and length approximately L with third iteration Sierpiński carpet electrodes and a weak link of width d ($d \ll L$). One instance of every boundary corresponding to a unit normal vector in Table 3.1 is marked with a black line. (b) Schematic of the rectangular junction. (c) Schematic of the non-fractal junction, with the same surface-to-hole ratio as the third order Sierpiński carpet, but with holes distributed equally along the y -axis.

nor fractal characteristics. The height of the second and third side lobes is seen to decrease slightly more rapidly for the fractal junction. The width of the side lobes, however, approaches the same asymptotic value, which is also observed in [3] for the rectangular junction. The phase along the y -axis of the right electrode is included in Figure 3.3b. As expected, it is similar for both devices.

Now we move on to the interplay between junction dimensions and periodicity. To establish a baseline and test the performance of the code, the periodicity of the interference pattern is first retrieved for the case of a rectangle of width L and

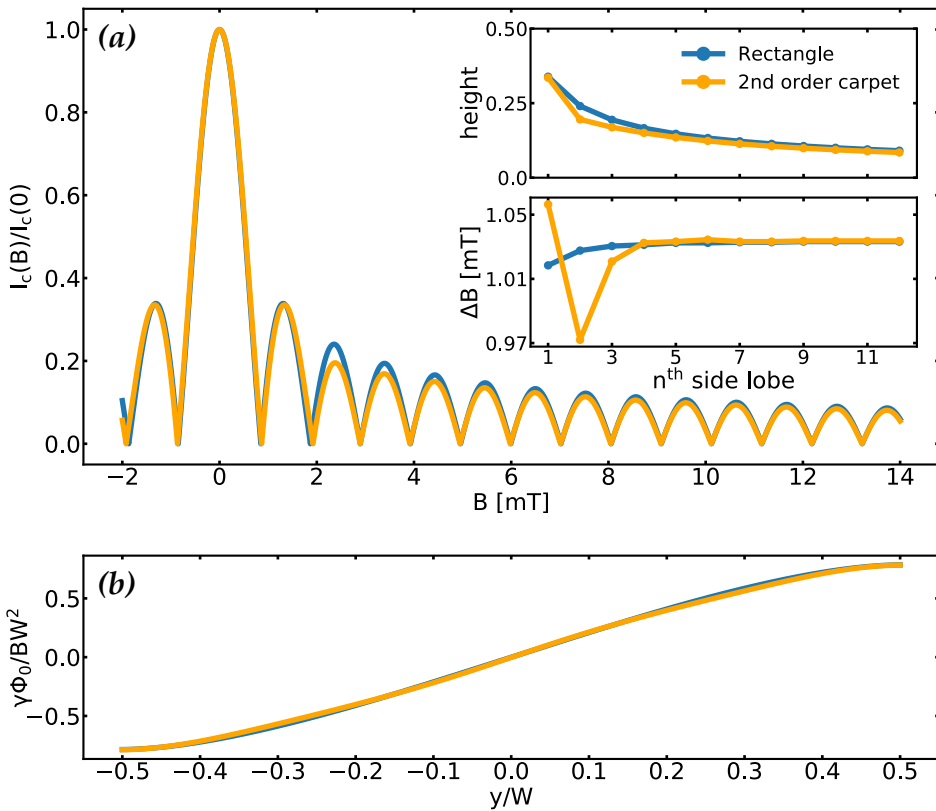


Figure 3.3: (a) Simulated interference pattern for the rectangular junction and the junction with second order Sierpiński carpet electrodes. Both junctions have $W = 2$ and $L = 4 \mu\text{m}$. The top inset shows the height of the n^{th} side lobe, while the lower inset shows the periodicity of the oscillations. Note that the interference patterns for both junctions look qualitatively similar, although the peak height seems to decay slightly faster for the fractal junction. The width of the side lobes increases to an asymptotic value for large n , which agrees with results from [3]. (b) Simulated gauge-covariant phase γ along the y -axis of the right electrode, normalized to $\gamma\Phi_0/BW^2$, with the applied magnetic field $B = 1 \text{ T}$. As can be expected from (a), the phase is similar for the rectangular and fractal junctions.

height W (with the junction bisecting the geometry widthwise) and compared to the result in [3]. Values for ΔB are scaled to the dimensionless quantity $\Delta BW^2/\Phi_0$ and are plotted as a function of the surface to width ratio A/W^2 (which, in the case of a rectangle, evaluates to L/W) where L is varied and W is fixed at $1 \mu\text{m}$. The resulting curve is displayed in Figure 3.4a. The asymptotes corresponding to the limits of ΔB for $L \ll W$ and $L \gg W$ are drawn as dotted lines. It is found that the code succeeds in replicating the periodicity relation for the rectangle as found in [3], including asymptotic behaviour.

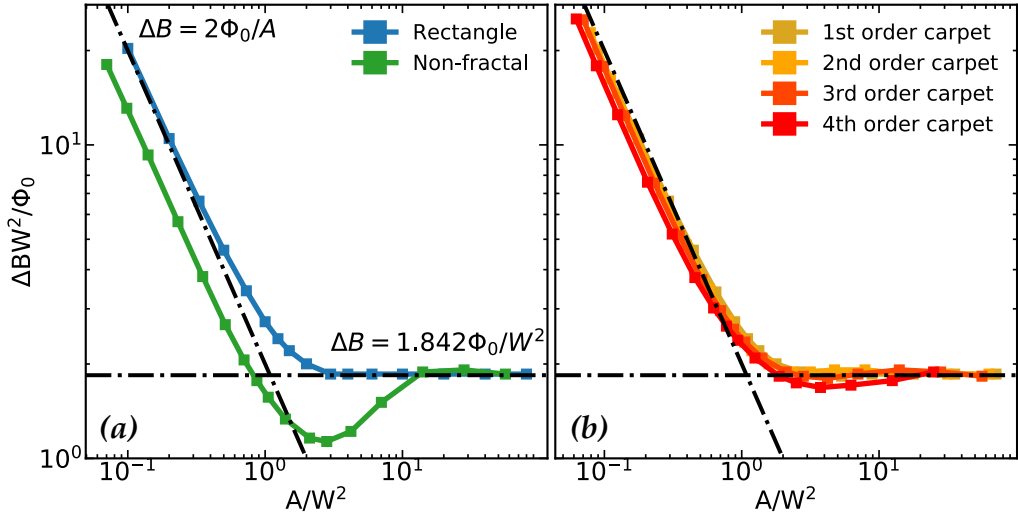


Figure 3.4: Dimensionless periodicity of the interference pattern versus surface to width ratio of the junction, with axes plotted on a log scale. In the computations, W has been fixed at $1\text{ }\mu\text{m}$ while L is varied. Dotted lines represent the asymptotic limits derived in [3]. (a) Note that the periodicity of the rectangular junction agrees with predictions by [3]. The non-fractal geometry has the same surface-to-hole ratio as a third order Sierpiński carpet, but with holes placed uniformly along the y -axis and not in a fractal pattern. Its periodicity converges to the horizontal asymptote for large values of ΔB but does not approach the left asymptote. In addition, the non-fractal geometry features a significant depression for intermediate values of A/W^2 . (b) Simulated periodicity for Sierpiński carpets of first, second, third and fourth order. Values converge to the horizontal asymptote, but disagree with the other asymptote: each increment in geometrical complexity introduces a larger offset. At the same time, a similar depression as in (a) is visible, increasing with fractal order but not reaching the level attained by the non-fractal geometry.

In the next step, the code is applied to the simulated phase distributions of four iterations of the Sierpiński carpet. Results are included in Figure 3.4b. For small ratios of A/W^2 , it is found that simulated phase distributions are increasingly affected by numerical limitations, which yields unpredictable, oscillatory behaviour in this limit. These results have been discarded by installing a suitable cutoff at $A/W^2 \sim 0.1$. The outliers likely originate from complications in the grid definition, as becomes clear upon inspection of the mesh. For large ratios of A/W^2 , the familiar asymptote is recovered. Some new effects emerge in the intermediate A/W^2 -regime. It appears that the periodicity of the interference pattern demonstrates a ‘dip’ for the geometries with holes at these intermediate values. The dip flattens out for lower iteration numbers of the fractal junctions, which agrees in-

tuitively with the notion that low-order Sierpiński carpets approach the geometry of a square (and, by extension, approximate a rectangular geometry, provided that the rectangle has $A/W^2 \simeq 1$).

It is readily observed that the area of the Sierpiński carpet scales with $8/9$, i.e. $a_i = (8/9)^i$, where i is the iteration number (with $i = 0$ corresponding to the unit square). It goes to zero as i goes to infinity: $\lim_{i \rightarrow \infty} a_i = 0$. A/W^2 -values in Figure 3.4 account for holes in the geometry.

As a way to assess the influence of fractality on the obtained pattern, the simulation is repeated for a geometry with the same surface-to-hole ratio as the third order Sierpiński carpet, but with non-fractal alignment of the holes: the ‘Non-fractal’ geometry in Figure 3.4a. The resulting curve has a much more pronounced dip and the offset with respect to the left asymptote is considerable. This discredits the notion that the dips, as well as the asymptotic offsets, observed in Figure 3.4b stem from the fractal nature of the geometry.

Experimental methods

In this chapter, steps in the fabrication of thin-film planar Josephson junctions with fractal electrodes are explained and the experimental method for measuring superconducting quantum interference patterns (SQI's) is described.

4.1 Nanofabrication procedure

4.1.1 Electron-beam lithography

The first step in preparing devices consisted of electron-beam lithography on a silicon wafer. Wafer details are listed in Table 4.1. The devices required 4 contact pads (to allow a 4-point measurement) connected by nanowires to a central stage where a junction was created. After some trial and error, it was agreed to use $200 \times 200 \mu\text{m}$ contact pads with $200 \mu\text{m}$ spacing, $28 \mu\text{m}$ wires and a $30 \times 40 \mu\text{m}$ central stage. Figure 4.1 shows the design of a single device. Twelve devices were fabricated per sample to provide leeway for tuning and mistakes.

Samples were cleaned in acetone and spin coated with a double layer PMMA-resist at 4000 rotations per minute. For the first layer, an AR-P 662.06 600K resist was applied, while for the second layer AR-P 672.045 950K was used. Spincoating was done with an SPS™ POLOS SPIN150i/200i infinite spin coater. After application of each layer, the sample was baked for 3 minutes at 150° .

Lithography was performed inside an EBPG Raith™-100 at a probe current of 2 nA and a beam current of approximately 12.5 nA, while the high voltage was fixed at 30 kHz and the emission current was measured to be 53 μA throughout

Table 4.1: Wafer properties.

Supplier	University Wafers	
Material	Silicon	
Type	P/B	
Resistivity	0.001-0.005	Ωcm
Coating	300	nm
	wet thermal oxide	
Orientation	<100>	
Polish	SSP	
Thickness	525	μm

the process. Using these settings and an area dose of $350 \mu\text{C}/\text{cm}^2$, a dwell time of approximately 0.018 ms and a beam speed of 14.10 mm/s were computed. Samples were checked for defects with an optical microscope.

4.1.2 Sputtering

The metal layers were produced by DC argon sputtering.* For the final device, four layers of material were deposited. From bottom to top: a 5 nm Ti sticking layer, a 60 nm Ag layer, a 55 nm MoGe layer and a 5 nm Ti capping layer. Thickness and layer composition were chosen initially to match [3] and were progressively adjusted on the basis of trial-and-error. The sticking layer was added after issues concerning the lift-off procedure because of weak attachment to the substrate. Initially, a 4 nm MoGe sticking layer was applied, but this practice was discontinued after many consecutive samples were found to perform inadequately: the sticking layer, despite its modest thickness, appeared to go superconducting below T_c , and this shorted the junction. It was later found that superconductivity inside MoGe thin films is not fully suppressed even for a thickness below 5 nm (c.f. [31]), thus validating our observations. The capping layer was deemed necessary to limit defects that are inflicted by the FIB (Subsection 4.1.3). The decision to add a capping layer was made simultaneously with the decision to switch to Ti sticking layers. Ti has $T_c = 0.4 \text{ K}$ [32, p. 8], which is far below the minimum temperature attained

*Sputtering was done on the Z-407 Automatic sputter system (home-built).

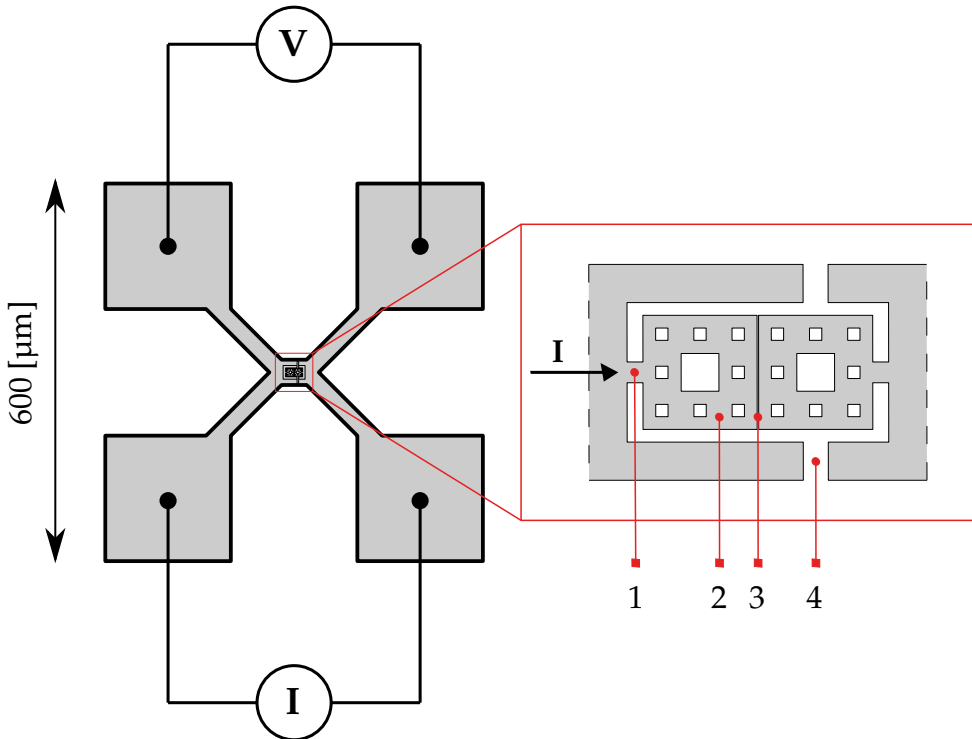


Figure 4.1: Schematic of a single device with a close-up of a fractal Josephson junction in the central stage area. The junction consists of two electrodes with a second order Sierpiński carpet structure (2), separated by a narrow weak link (3). A trench (4) bisects the device such that current is forced through the constrictions (1), into the junction. Wires bonded to the contact pads allow a four-point measurement of current and voltage. The size of the junction is around $2 \times 4 \mu\text{m}$ and has been exaggerated with respect to the rest of the device.

in our experiments ($\sim 2.3 \text{ K}$), and does therefore not short the junction. In this light, it is not decisive whether one or the other, or both of the interventions are critical in producing working junctions. Sputtertimes for the layers were calculated based on indicated sputter rates which turned out to be 100, 150, 589 and 100 s, respectively. Sputtering was performed without intervals for cooldown but with a presputtertime of 120 s for each layer. After sputtering, samples were put in acetone for approximately 20 hours. The remnants of the resist film were then carefully removed (lift-off). Table 4.2 provides an overview of the specifications of the sputtering process for the final device, while Figure 4.2 shows a step-by-step depiction of the lithography and sputtering steps.

Table 4.2: Sputter sequence for the final device. The order of deposition is bottom to top, with the entry in the last row corresponding to the first deposition (i.e. the layer directly on top of the substrate).

Layer	Thickness (nm)	Sputtertime (s)	Presputtertime (s)
Ti	5	100	120
Ag	60	150	120
MoGe	55	589	120
Ti	5	100	120

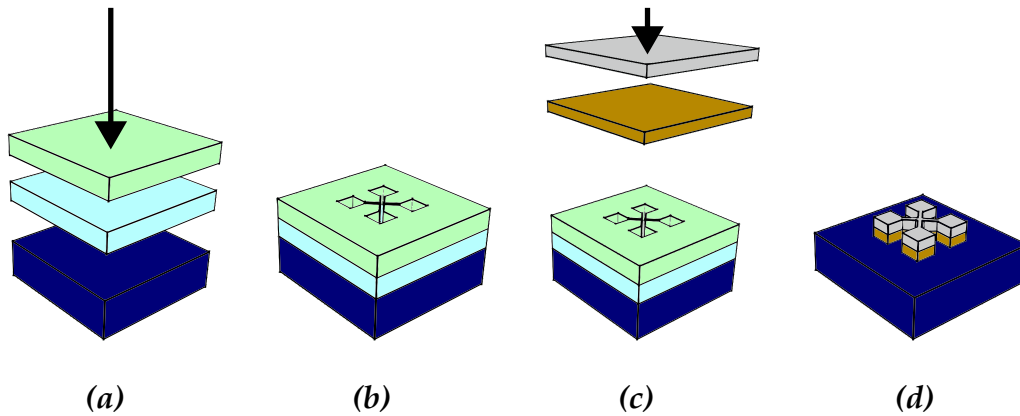


Figure 4.2: Nanofabrication procedure for a typical device with four contact pads and wires to a central stage (Figure 4.1). (a) A silicon wafer (dark blue) is spin-coated with a PMMA-resist solution. In this example, two layers are applied (light blue and green). (b) The pattern is e-beamed on top of the resist. Exposure to the high energy electron beam locally destroys the resist. To develop the structure, the film is treated with a solvent of MIBK mixed with isopropyl to remove resist in the affected area. This leaves a mask of resist surrounding the device. (c) One or more metals are sputtered on top of the substrate. On places where the resist has vanished, metals are deposited directly on top of the substrate, while elsewhere, metals are deposited on top of the PMMA. (d) During lift-off, the mask is dissolved in a solution of acetone; the deposited metal bilayer emerges in the desired shape. The device is now ready for structuring: the act of milling fine (sub-micrometer) details into the metal layer with a focused ion beam (FIB) to produce the junction (see e.g. Figure 5.3).

4.1.3 Focused ion beam

In the final step of the nanofabrication procedure, the actual junction is realized on the stage area of the devices. This step is called ‘structuring’ and was accomplished through milling of the sputtered layers with a focused ion beam (FIB). The FIB installation uses a beam of Gallium (Ga) ions to cut submicron details into the deposited metal layers. FIB on all devices was performed with an Aquilos™ Cryo-FIB leased from NeCEN (Netherlands Centre for Electron Nanoscopy) in Leiden.

4.2 Measurement procedure

RT-measurements and IV-sweeps with varying magnetic field were initially conducted inside a DynaCool™ PPMS at cryogenic temperatures. Field sweeps were performed in the range of -15 tot 15 mT with 0.05 mT increments. The stability of the magnetic field produced by the magnet controller of the PPMS was however insufficient for the purpose of the experiment, because of strong feedback response. Figure 4.3 shows that the field oscillates around a setpoint $B = 0$ with an amplitude that is similar to the desired resolution of the field sweep (0.05 mT). For this reason, the experiment was transferred to the Vectormagnet, which can generate more stable fields. It was also decided to carry out AC-measurements because of the improved signal to noise ratio. The AC-measurements were performed with a Synktek Lock-in Amplifier.

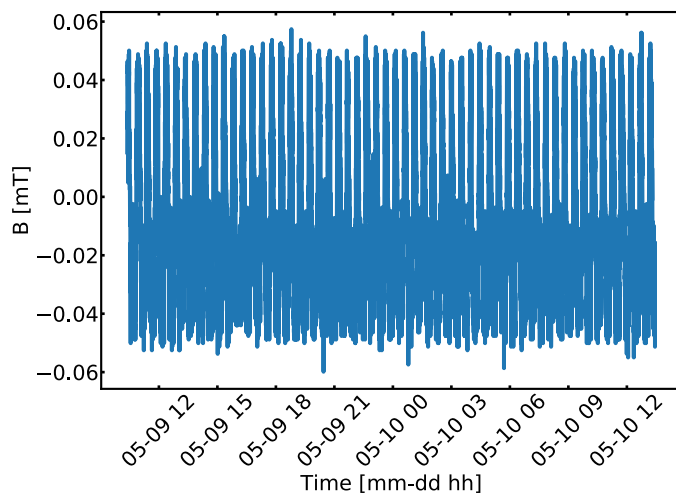


Figure 4.3: Instability of the magnetic field generated by the PPMS. Data represents a test measurement over a span of multiple days, with setpoint $B = 0$. The range of oscillations (~ 0.1 mT) is approximately twice the desired resolution of the field sweep: 0.05 mT.

Chapter **5**

Measuring Sierpiński carpet Josephson junctions

In order to experimentally test the devices simulated in Chapter 3, we fabricated SNS Josephson junctions with rectangular and with second order Sierpiński carpet electrodes. Functional devices were produced only after two major problems had been tackled:

1. Weak attachment to the substrate, resulting in destruction of the devices during lift-off;
2. Finding an adequate composition of layers.

The first problem was approached in two ways. On the lithography side, the sensitive parts of the device were executed more sturdily by upscaling the dimensions of the wires connecting the contact pads to the stage area, and by increasing the size of the stage area itself. Compared to the first design, the thickness of wires was almost tripled (10 to 28 μm) and the size of the stage area was more than doubled (from 10×20 to 30×40 μm). On the deposition side, a sticking layer was added to the design. A sticking layer (also known as an adhesive layer) improves the bonding between film and substrate. Initially, a 4 nm MoGe layer was added, but later on the change was made to 5 nm Ti for reasons outlined in Subsection 4.1.2. This connects to the second problem: choosing an appropriate layer composition. The initial choice of layers matched the design in [3], where 55 nm MoGe was deposited on 20 nm Ag without the use of additional layers. When it appeared that none of the devices worked, the thickness of the Ag-layer was increased to 60 nm, to mill deeper junctions. In a final batch, a 5 nm Ti capping layer was added to avert the possibility of malfunctions due to FIB damage (by stray ions colliding

with critical parts of the sample). This occurred simultaneously with the transition to 5 nm Ti sticking layers. Measurements obtained on these devices are the topic of the next sections.

5.1 FIB results

The choice of junction length and width, apart from their relative value, is also important in the absolute sense since the periodicity ΔB is inversely proportional to $\max\{\gamma/B\}$ (eq. (3.9)), and $\max\{\gamma\}$ is proportional to W and L . Ultimately, ΔB should not become smaller than the resolution of our measurements. The drawback of choosing W and L small, however, is that structuring becomes increasingly difficult below certain sizes. This essentially turns choosing a suitable W and L into an optimization problem.

Exploratory tests with the FIB demonstrated that a second order Sierpiński carpet could be accurately produced within system limitations, while the smallest holes in a third order carpet (~ 70 nm) suffered from non-uniformity in size and featured considerable deformations around the edges, illustrated by Figure 5.1. It was therefore decided to structure second order fractal electrodes. In addition, a regular (unperforated) rectangular junction was structured to compare junction performance with known results by [3] among others. The two devices will henceforth be referred to as the ‘fractal’ and the ‘regular’ device. The parameter which controls milling depth (z-size) was set to 0.17 μm for the narrow link, while the central hole was milled with a z-size of 0.07 μm and the smaller holes with 0.12 μm . At these depths, the superconducting MoGe-layer was severed and the non-superconducting Ag exposed, creating the weak link.

Figure 5.2 shows false-color images of the fractal junction and the rectangular junction captured with the SEM installed inside the FIB. Figure 5.3 shows a top view (false-color) SEM-image of the fractal junction. Important dimensions are annotated with white bars. The electrodes of the fractal junction have been analysed with FracLac for ImageJ and were found to have box-counting dimension $D = 1.8 \pm 0.04$. The realized electrodes match the desired fractal dimension quite well; any deviation from the Hausdorff dimension (approximately 5%) is readily explained by slight irregularities and defects in the pattern.

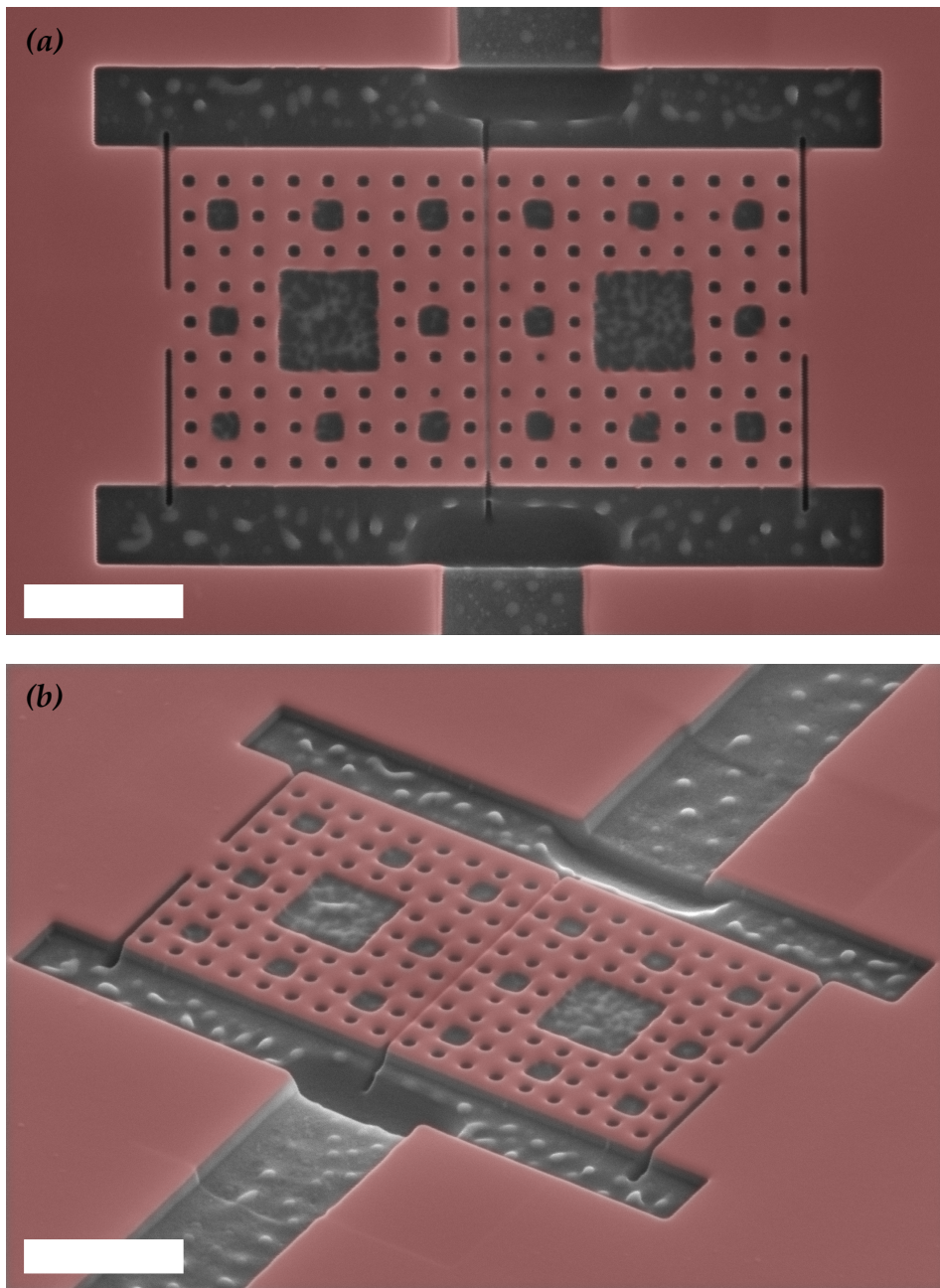


Figure 5.1: False-color SEM-images of a planar Josephson junction with third order Sierpiński carpet electrodes. The scale bar corresponds to 1 μm . (a) Take note of the defects appearing in holes of the third order (the smallest holes), that have sides of approximately 70 nm: the hole shape resembles a circle and the size is non-uniform. (b) The weak link also suffers damage from holes in its direct proximity.

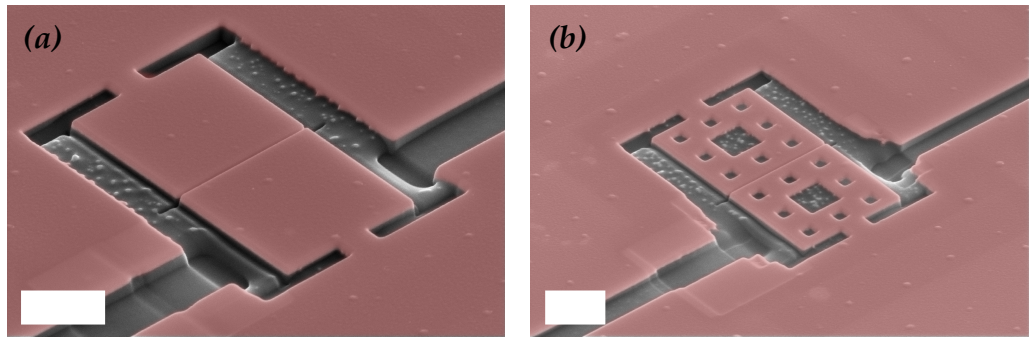


Figure 5.2: Side view, false-color SEM-images of the junctions. The scale bar corresponds to 1 μm . (a) Rectangular junction. (b) Fractal junction.

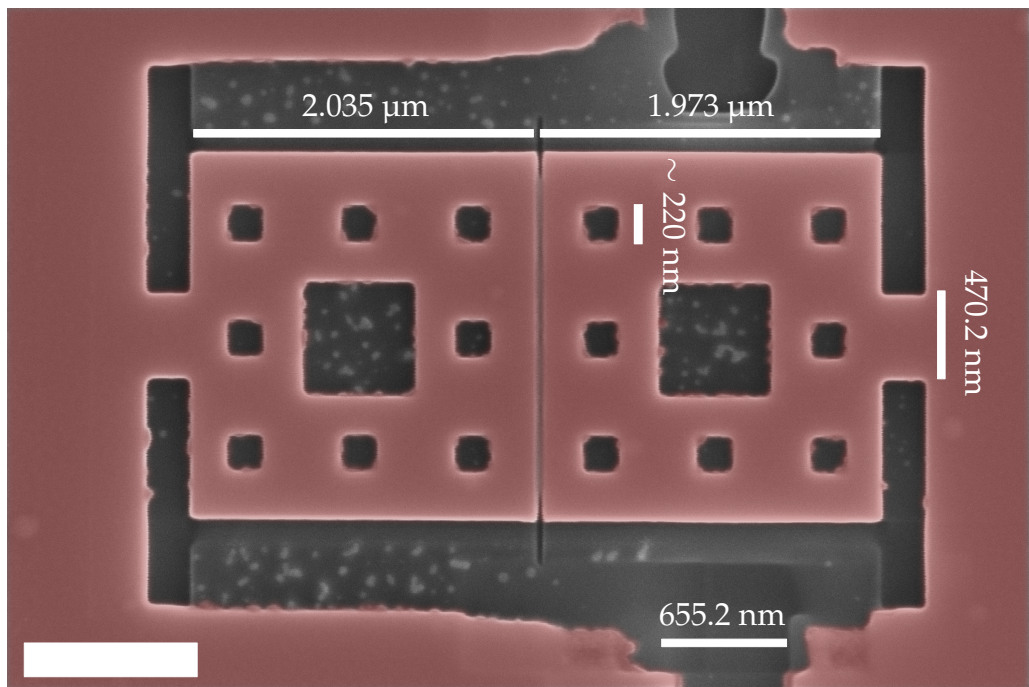


Figure 5.3: Top view, false-color SEM-image of the fractal device used for SQI measurements: an SNS-Josephson junction with second order Sierpiński carpet electrodes. The scale bar corresponds to 1 μm . Important length scales are also indicated with white bars. The central hole has sides of approximately 660 nm, while the small (second order) holes are around 220 nm. The geometry for both the right and left electrodes was found to have box-counting dimension $D = 1.8 \pm 0.04$.

5.2 Resistance versus temperature

Before using the devices to record superconducting quantum interference patterns (SQI's), it is essential to establish whether they contain functional junctions. For this to be the case, we require superconducting transitions to occur at low enough temperatures. Figure 5.4 shows the resistance versus temperature characteristic of the devices. Two transitions are visible: an initial transition at higher temperatures (~ 6.0 [K]) that corresponds to the superconducting transition of the electrodes, and a second transition (~ 4.5 K) corresponding to the transition of the junction. The rectangular junction appears to retain a tiny but notable amount of residual resistance; it is assumed that this represents an artefact of lock-in measurements rather than a physical effect. The normal-state resistance of the fractal junction is higher because of the reduced lateral surface area due to the structure in the film. Transitions of the fractal junction are shifted to a slightly lower temperature with respect to the transitions of the rectangular junction, possibly because this higher resistance generates additional dissipation which contributes to heating.

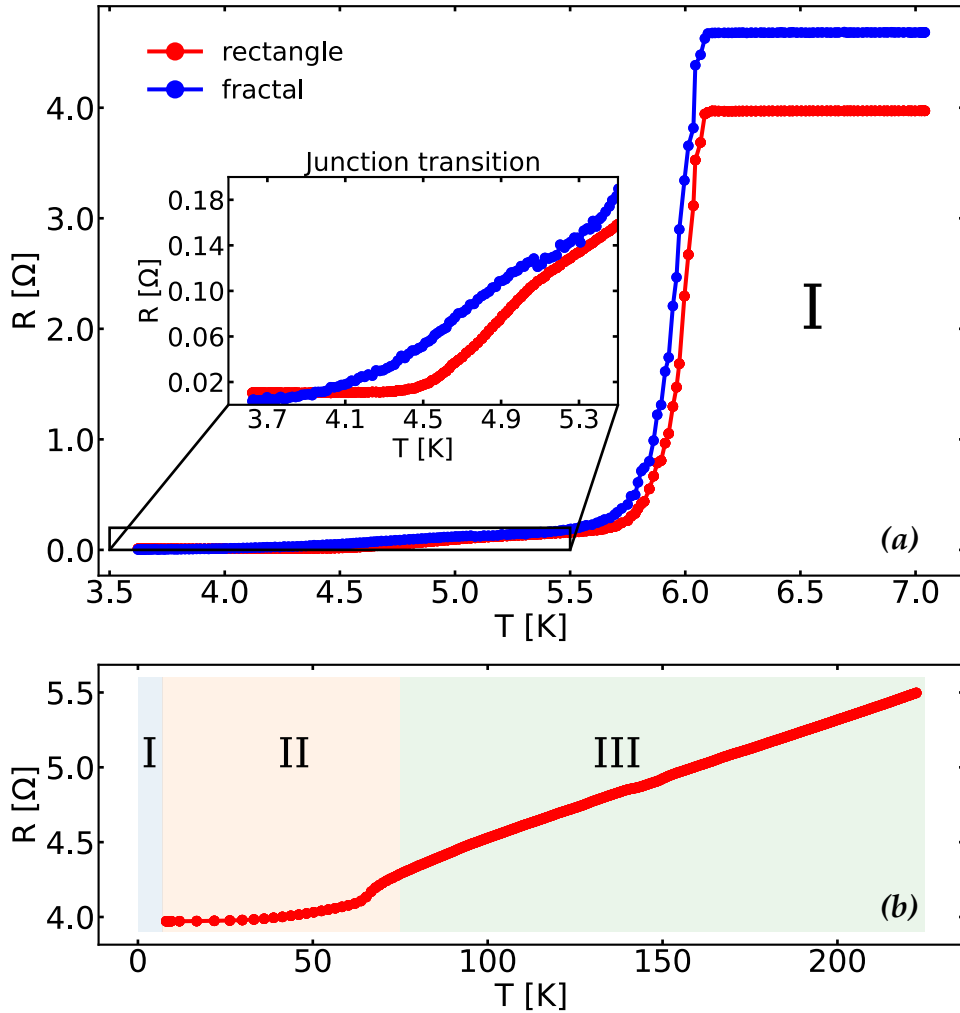


Figure 5.4: RT-characteristics of the rectangular and the fractal junction. (a) Transition to the superconducting state is manifested in two stages: a large drop in resistance occurs when the electrodes become superconducting ($T_c \sim 6.0$ K; the junctions remain in the normal state), while the attenuation of residual resistance (dV/dI drops to zero) takes place once the junctions go superconducting ($T_c \sim 4.5$ K; inset). Note the higher normal-state resistance encountered in the fractal junction, which is readily explained by the presence of holes. The rectangular junction also seems to retain a small but noticeable residual resistance even at the lowest temperatures. This is thought to be an artefact of measuring with the lock-in. (b) Resistance versus temperature for the rectangular device, spanning the full temperature range of the cooldown. Three regimes have been marked, denoted by Roman numerals. In region III, the resistance decreases linearly with temperature. In region II, resistance takes a sharp downturn and then decreases slowly. Superconductivity develops in region I.

5.3 Rectangular junction

Figure 5.5 presents the SQI of the rectangular junction at 2.3 K. The field sweep was recorded in two parts to reduce measurement time, and both datasets were combined afterwards.

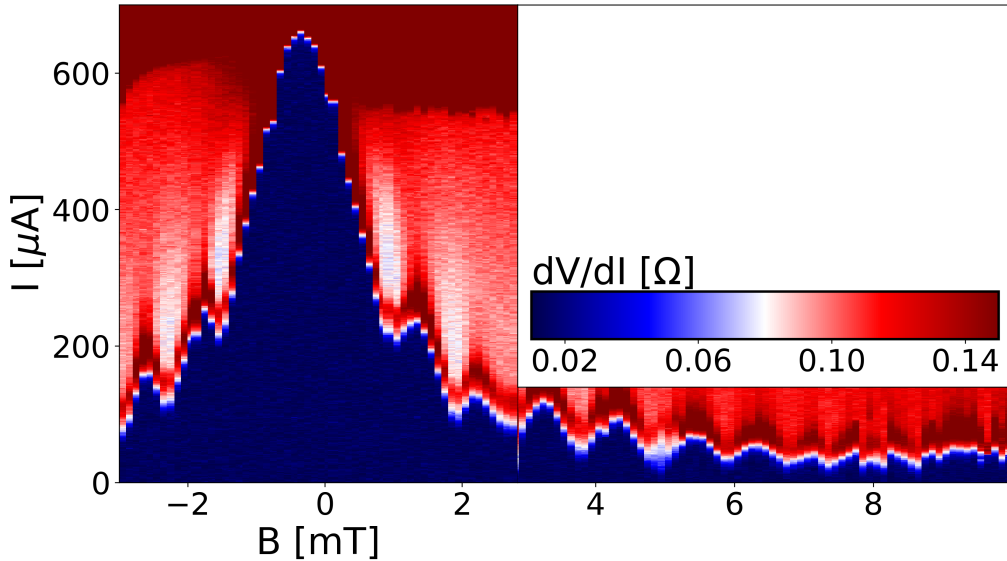


Figure 5.5: SQI corresponding to the rectangular junction at 2.3 K. The SQI represents a differential, 2-point resistance dV/dI derived from a sequence of IV-measurements at distinct values of the applied magnetic field (B). Take note of the familiar Fraunhofer-like pattern. Measurement time was reduced by limiting the probe current above 3 mT.

In order to confirm that we can reliably fabricate planar Josephson junctions and as a comparison to our fractal junction, we record the SQI-pattern of the regular, rectangular junction. The general shape of the SQI assumes the Fraunhofer-like pattern conventional to thin-film planar Josephson junctions. From Figure 3.3, we expect the periodicity of the fifth side lobe of the interference pattern to be approximately 1.0 mT. Furthermore, [33] suggests that the modulation of the magnetic field in planar junctions follows $\Delta B = 1.8\Phi_0/W^2$, from which we find (for our junction with $W = 2 \mu\text{m}$) $\Delta B \sim 0.9 \text{ mT}$. Both predictions appear to agree reasonably well with the observed periodicity of the fifth side lobe, which is approximately 1.0 mT. The central peak, in contrast, is exceedingly wide. From literature, we know that $I_c(B)$ is modulated if the junction is either in the *long* or *short* junction limit. The governing quantity in this regard is the Josephson penetration length λ_J , which dictates the characteristic length scale for magnetic field penetration into the

junction – as opposed to ‘regular’ λ , which pertains to the electrodes. For long junctions, most sources quote $W > \lambda_J$ (with W the junction width) [34], although this is not a strict definition, since for example [33] quotes $W > 4\lambda_J$ for long junctions and $W \leq \lambda_J$ for the short junction limit. Long junctions are able to screen the applied magnetic field within the junction up to the Josephson lower critical field H_{c1J} , after which so-called ‘Josephson vortices’ penetrate into the junction. The resulting central lobe is wider and decreases linearly with field [33]. To demonstrate that we are in the long junction limit, we use $\lambda_J = \Phi_0 t_{junc} W / 4\pi\mu_0\lambda^2 I_c(0)$ with t_{junc} the thickness of the junction (not the superconducting film). $\lambda_L(0)$ for a-MoGe is known to be 700 nm [35]. Adjusting for temperature $T = 2.3$ K and $T_c = 6.5$ K with eq. (2.11) and using $t_{junc} = 2$ μm and $I_c(0) = 650$ μA , $\lambda_J \sim 1.6$ μm and we see that $W > \lambda_J$ such that we are inside the long junction limit [33]. We also calculate Λ using the definition in Section 2.3 and see that it is approximately 4.5. This means that the applied magnetic field and the screening currents are decoupled, which agrees with the thin-film limit.

All in all, the rectangular junction seems to meet performance expectations for a long, planar Josephson junction. This provides a reassuring background for testing the fractal device.

5.4 Fractal junction

We are now in the position to turn our attention to the fractal junction.

5.4.1 Vortex trapping effects

Contrary to the regular junction, the fractal junction shows a far more unconventional SQI-pattern. Two SQI's of the fractal junction at 2.3 K are shown in Figure 5.6.

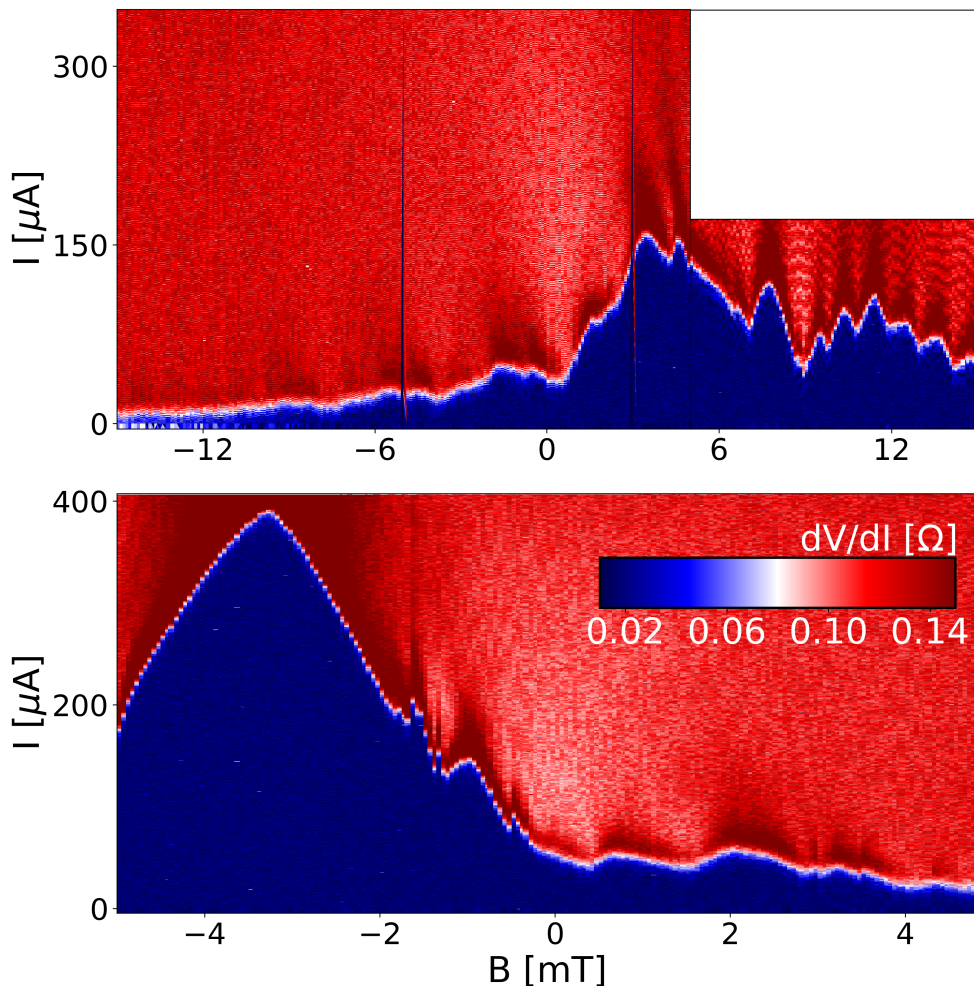


Figure 5.6: SQI's corresponding to the fractal junction at 2.3 K. The pattern is not reproducible and is highly irregular and asymmetric.

The SQI's in Figure 5.6 are exemplary in demonstrating three key features that recurred in all measurements on the fractal device. Firstly, the maximum of the critical current distribution is seen to be strongly offset with respect to zero field. Secondly, the central peak is extremely broad, much more so than the central peak of the rectangular junction (which is already considerable, due to the device being in the long junction limit). The periodicity of visible oscillations, on the other hand, is irregular and cannot be tied to a specific scale. Lastly, the pattern is irreproducible, as becomes immediately clear upon inspection of Figure 5.6a in relation to 5.6b. In particular, the SQI-pattern was seen to vary across measurements as a function of the maximum current range, the cooldown rate, the polarity of the current and the applied field. In the remainder of this section, it is argued that these variations are in fact attributable to vortex trapping events. During the course of the research project, another explanation was hypothesized drawing on the possibility of superconductivity itself being impaired under certain circumstances in MoGe thin films, owing to phase fluctuations. However, any suspicion of this kind was discarded after studying [31], where it is put forth that such effects only surface strongly in films less than 5 nm thick.

Figure 5.7 shows various IV-curves pertaining to the fractal device, taken at 2.3 K. The IV's are obtained with two current polarities: a 'forward' measurement from negative to positive currents and a 'backward' measurement from positive to negative currents (see figure). Panels in the same row show measurements conducted without intermittent reheating of the sample, while between the two rows, the sample temperature is raised above T_c to remove trapped vortices. The perceived vortex trapping events are marked with a black arrow. They are characterized by a sudden change in voltage, which is attributed to two mechanisms:

- A trapped vortex redistributes the phase in its vicinity and thereby changes shielding currents;
- The vortex modifies the field locally and this corresponds to a translation in the SQI-pattern, and therefore to a change in the IV-curve.

The key observation is that trapping of a vortex creates a new stable trajectory for the IV-curve, which is maintained until the next vortex entry. At the same time, the results do not support evidence for a hysteretic property that is intrinsic to the fractal device: in the absence of trapping events, Figure 5.7a demonstrates that the backward and forward polarities follow the same curve. Vortex trapping thus accounts for sudden jumps in some of the IV-curves and offers a consistent explanation for changes in their trajectories, while an hysteretic motivation fails to explain these phenomena.

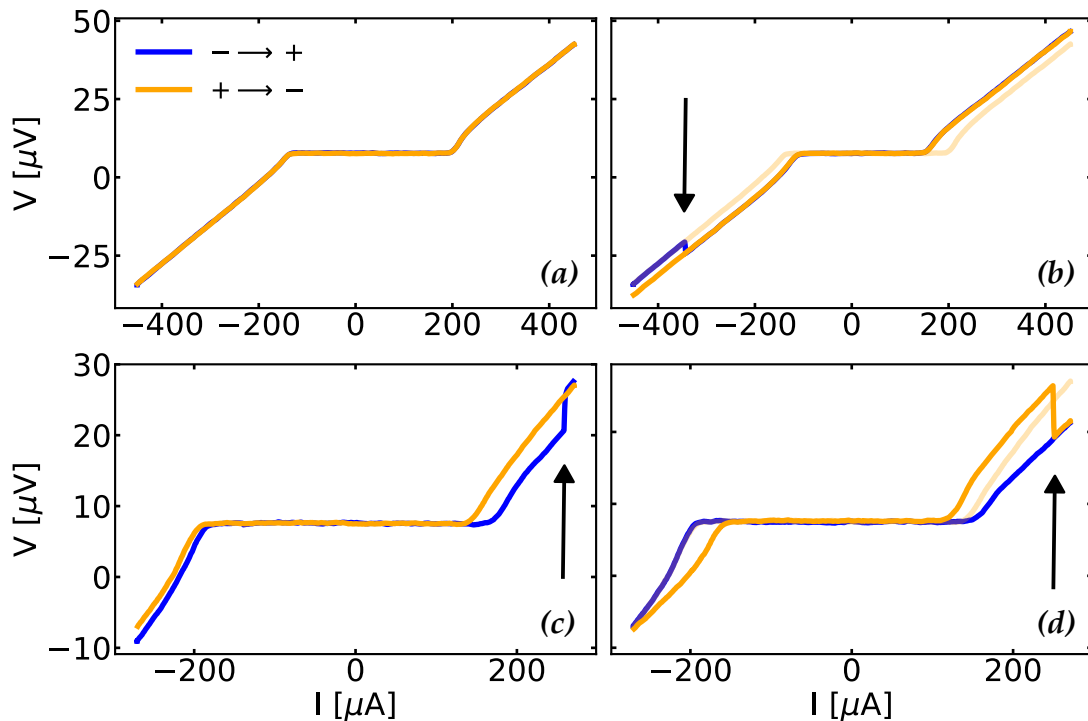


Figure 5.7: IV-curves at 2.3 K, recorded with two current polarities: a measurement from negative to positive currents ('forward'; $- \rightarrow +$) followed by a positive to negative measurement ('backward'; $+ \rightarrow -$). Vortex trapping events are indicated with black arrows. Between the rows, the sample was heated to 7 K ($> T_c$) to destroy any lingering vortices. (a) No vortex trapping: the forward and backward measurements coincide. (b) A vortex is trapped near the start of the forward measurement. The first part of the forward measurement agrees with the backward measurement from (a), shown with a transparent line in the same plot. Immediately after the vortex is trapped, the IV is pushed into a new stable trajectory, which is not broken until a new vortex enters. (c) A vortex enters at the end of the forward measurement. (d) Initially, the forward measurement corresponds with the backward measurement from (c). After the zero resistance state, the two curves are shown to diverge, indicating the possibility of a vortex entering unobserved in the superconducting regime.

Before moving on to the next section to continue the main line of reasoning, we note that the fractal junction had a simulated periodicity of approximately 1.0 mT (Figure 3.3). It is however evident from the SQI that no such (simple) periodic dependence exists, but that the interference pattern rather includes the contribution of many harmonics with varying period.

5.4.2 Isolating the contribution of geometry

In the previous section, detected anomalies in the fractal SQI's were attributed to vortex trapping events. The impact of vortex trapping on the interference pattern is such that geometrical effects – that is, any hypothetical contribution originating in the fractal structure of the electrodes – are obscured. It is therefore desirable to explore ways to eliminate vortex trapping. A remedy was found in a combination of adaptations to the measurement setup: limiting the current through the junction while also increasing the temperature of the sample to lower the critical current threshold. Evading high probe currents has been found to effectively prevent vortex entries. In particular, no vortices have been observed entering below approximately 50 μA . Apart from a single instance, all observed vortices entered at currents exceeding 100 μA . Figure 5.8 presents the SQI after implementing said adaptations. For this measurement, the current range has been limited from 0 to 70 μA . A sample temperature of 3.5 K (instead of the previous 2.3 K) was found to limit critical currents to the probe current range. It is worth mentioning that the same SQI was recreated with substantial accuracy after heating the sample above T_c and recooling, indicating a stability that was absent in any measurement affected by (random) vortex entry events. By looking also at the high degree of symmetry and regularity, it is presumed that Figure 5.8 represents the geometry-dominated critical current interference pattern.

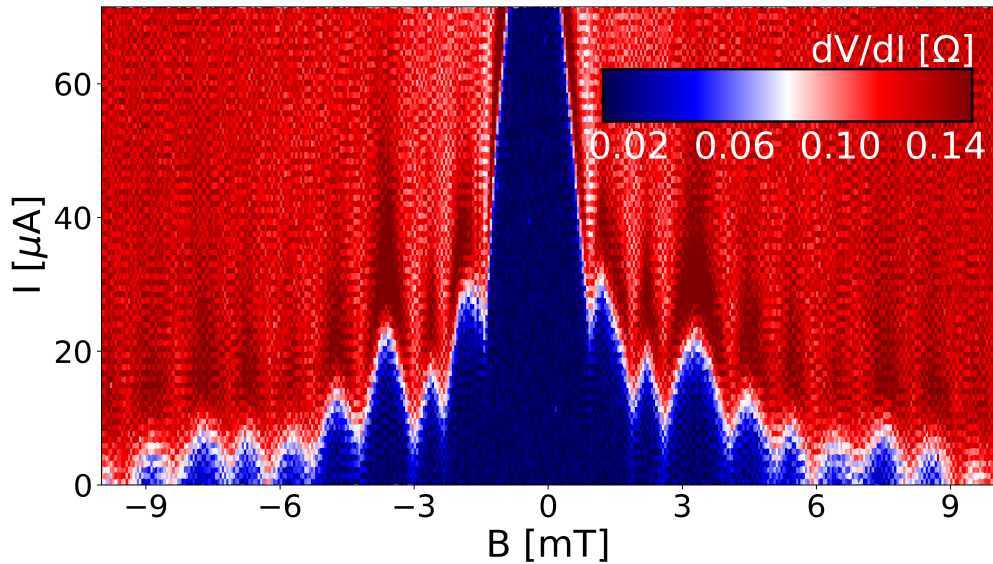


Figure 5.8: SQI of the fractal junction at 3.5 K after reheating to 7 K and a slow cooldown with 0.1 K/min.

We conclude the analysis by evaluating the spatial critical current distribution $J_c(y)$ over the fractal junction by following the steps in [3, 8]. Recall that $J_c(y)$ is related to $I_c(B)$ through the Fourier transform (Section 3.1). The computed distribution is displayed in Figure 5.9. Approximate locations of holes along the y-axis of the fractal junction are marked by shaded areas and are seen to coincide with dips in $J_c(y)$. To test whether this is a fractal effect, it would be beneficial to compare the distribution with a non-fractal geometry featuring random hole placement. A straightforward explanation that is not grounded in fractal effects would be that holes near the electrode boundary introduce local defects that impede current flow in these areas.

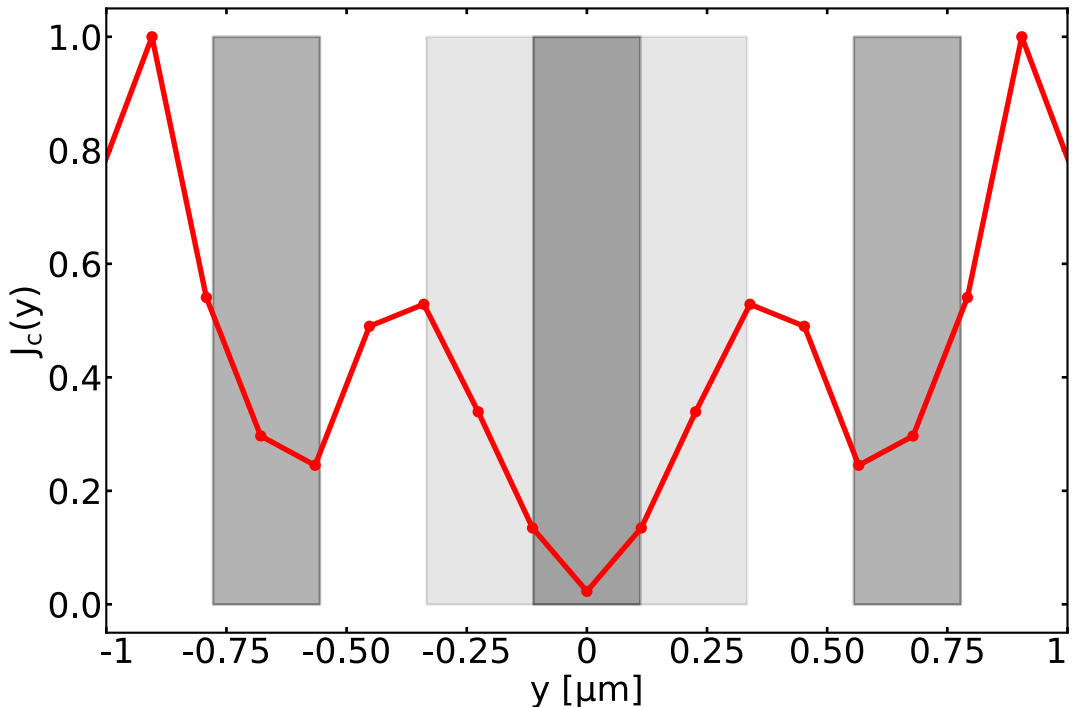


Figure 5.9: Distribution of the normalized critical current $J_c(y)$ along the y-axis of the fractal junction. Filled areas mark the locations of holes, with the dark rectangles indicating 2nd order holes ($\sim 2/9 \mu\text{m}$ across) and the light surface indicating the central, 1st order hole ($\sim 2/3 \mu\text{m}$ across). Dips in $J_c(y)$ coincide with the location of holes.

Conclusion and outlook

In the previous chapter, we were able to find a superconducting interference pattern for a planar Josephson junction with fractal electrodes, that could be attributed predominantly to the geometrical character of the junction. This was accomplished through an effective suppression of random vortex entries by choosing a suitable probe current range and sample temperature. It was found that such a critical current pattern is reproduceable, symmetric and regular, but deviates strongly from the Fraunhofer-like distribution for planar rectangular junctions and does not agree with simulations. Depressions in the critical current $J_c(y)$ transverse to the junction axis were seen to coincide with the positions of holes in the geometry, but further research is necessary to attribute this effect to the fractal nature of the junction.

Having thus tasted the rich physical implications of a self-invariant geometry for the proximity effect in Josephson junctions has given ample reason to explore many untouched opportunities relating to research topics within the field of junction physics. In the rest of this chapter, we will cover an outlook of possible directions to undertake future endeavours. Some of the suggestions materialized quite naturally during the course of our proceedings and seem to harbour low-hanging fruit ripe for picking, while others emerged more slowly as the challenges encountered during our study prompted new questions, and these started to arrange as clues to unidentified crosslinks in a puzzle spanning multiple domains. This last group ought perhaps to be approached more tentatively, but may also hold the most striking surprises.

A problem most readily approached is to observe elementary characteristics of fractal junctions. One such example is to study the superconductor-normal phase

boundary for fractal structures. [36] investigates the $T_c(\Phi/\Phi_0)$ -curves for a network of Sierpiński gasket wires, and finds up to four orders of dilational invariance. Results are in agreement with a theoretical model by [37]. Future experiments could focus on mapping the $H_c(\Phi/\Phi_0)$ or $M(H)$ -distributions.

A logical stride in the direction of prospective research that involves both a continuation of our investigation into geometrical implications, and touches upon vortex pinning, is a study of the commensurability effect in arrays of superconducting dots. It has been demonstrated that at distinct values of the applied magnetic field, a geometric matching between the vortex lattice and the (quasi-periodic) potential induced by the underlying geometry of the lattice ensues, resulting in what is known as a *commensurate* state. Physically, a slowdown of the vortex lattice motion is realized, which prompts minima to appear in the magnetoresistance $R(H)$ at integer multiples of a primary commensurate field H_1 [38, 39]:

$$H_{match}(n) = nH_1, \quad n \in \mathbb{N} \quad (6.1)$$

This effect was observed by [38] and [39] in arrays of Nb triangles (submicron scale) on Si-substrate, overlaid with a Nb-film. [40] applies vortex pinning to a quasiperiodic pentagonal fractal array (referred to as a ‘Penrose’ array). The magnetoresistance in the mixed state shows a series of quasiperiodic minima which suggests that the vortex lattice and the self-similar structure of the array show correspondence at the various length scales present in the geometry: the inter-dot distance and the progressively larger (but self-similar) pentagonal composite structures that emerge from many individual dots. The quintessential implication is that the correlations stabilizing the quasiperiodic vortex lattice work over lengthscales long enough to overcome the energy penalty due to the deviation of the vortex lattice from the natural periodic order [41]. Continuing on the work of [40] could involve carrying out the experiment under transport conditions, aside from the many possible variations in the fractal structure of the array, ranging from modifying interdot distance to changing fractal type.

A second direction of expansion concerns the study of ratchet effects. It is well known that the motion of vortices can be strongly influenced by manipulating the underlying pinning potential. So-called ‘ratchet potentials’ are a peculiar instance of a pinning potential whose asymmetric and periodic properties allow unidirectional transport of vortices in the presence of an unbiased fluctuating drive. [42] shows that voltage rectification in an array of asymmetric antidots is induced by the intrinsic asymmetry in the pinning potential created by the antidots, whereas rectification in an array of symmetric antidots can be induced by applying a dc

bias. The controllable motion of vortices by means of the ratchet effect in experiments performed on superconducting samples with periodic arrays of asymmetric pinning centers is further demonstrated by [43]. Fractal geometries offer a logical extension to this framework because their periodicity is manifested on multiple spatial scales.

A slightly more adventurous suggestion would be to investigate giant Shapiro steps in networks of fractal structures. Giant Shapiro steps are the Josephson junction *array* equivalent of ‘regular’ Shapiro steps found in single junctions subject to radio-frequency (rf) excitation (see, for example, [8, pp. 23-24]). In a Josephson Junction array with an rf input current in zero applied field, the spacing of the giant Shapiro steps follows [44]:

$$V_n = n \left(\frac{Nh\nu}{2e} \right), \quad n = 0, 1, 2, \dots \quad (6.2)$$

When both an rf-current and a magnetic field are applied perpendicular to the array, *fractional* giant Shapiro steps appear when the applied magnetic field produces a commensurate state as a result of phase-locking between the rf-signal and vortex motion. Prominent commensurate states in a square array are visible when the number of flux quanta per unit cell, expressed as the rational quotient (frustration parameter) $f = p/q$ (with $p, q \in \mathbb{N}$), takes on values $f = \frac{1}{4}, \frac{1}{3}, \frac{1}{2}, \frac{2}{3}, \dots$ (note the symmetry about $f = \frac{1}{2}$). Corresponding fractional giant steps are distributed at voltages:

$$V_n = n \left(\frac{Nh\nu}{2qe} \right), \quad n = 0, 1, 2, \dots \quad (6.3)$$

[45] generalize a model by [46], and find additional fractional steps at $\langle V \rangle = Nh\nu/4e$. While these extra fractions are not visible in the results obtained by [44], they could be observed if experiments are conducted at lower temperatures, with less disorder, or with a different ac amplitude or frequency. Using fractal geometries to build the junction arrays – either by constructing junctions with fractal electrodes or by shaping the total array to resemble a fractal pattern – would take the search for new fractal giant Shapiro steps beyond existing boundaries. Even excluding Shapiro steps altogether, however, junction arrays in fractal configurations are a promising subject of study, since their physical behaviour has been shown to be sensitive to geometrical effects (e.g. consider the skewed current phase relationship and a collective frequency response in anisotropic junction arrays found in [47]).

Junction physics: some derivations

In this appendix, I derive (3.2), which is eq. (12) in [3]. Then, I will briefly discuss an adaptation of the formalism to include asymmetric electrodes. The derivation presented in this appendix aims to bridge gaps in understanding the necessary steps to compute the phase difference over the junction, and provides a detailed transition to eq. (3.2). This section started out as a set of personal notes, but because I considered much of the material non-trivial for readers not familiar with the topic, I instead opted to accommodate the key points in an appendix.

A.1 Derivation of (3.2)

We start our discussion by imagining a junction of width W and thickness t_{junc} , stretching along the x -axis, with the magnetic field in the z -direction and with a weak link spanning a distance d (see Figure 3.1). Note that \mathbf{B} remains invariant under the addition of an arbitrary gradient function to \mathbf{A} , because of the gauge freedom associated with the vector potential. We can exploit this property to fix $A_y = 0$ as this will simplify calculations. We then commence the derivation by recognizing that the gauge-covariant phase difference γ in the junction is related to the gauge-invariant phase gradient θ , which is the quantity between brackets in eq. (2.10), through the integral:

$$\varphi(y) = \int_{-d/2}^{d/2} \theta_x dx \quad (\text{A.1})$$

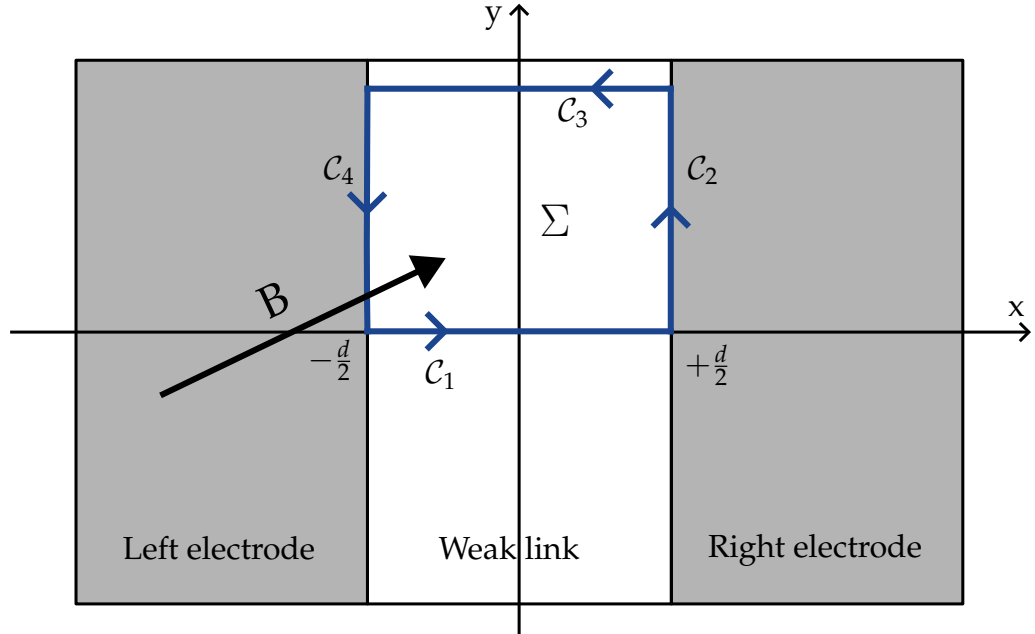


Figure A.1: Integration loop (blue) of width d and height y tracing the edges of the weak link. Σ is the surface enclosed by the loop. The applied field is pointing into the paper (the 'z' direction).

This is just the gradient theorem applied to θ . Substituting $\theta = (2\pi\mathbf{A}/\Phi_0 + \nabla\gamma)$ with $A_y = 0$ we get:

$$\varphi(y) = \int_{-d/2}^{d/2} \left(\frac{2\pi}{\Phi_0} A_x(x, y) + \frac{\partial}{\partial x} \gamma(x, y) \right) dx \quad (\text{A.2})$$

Note also that the integral over the derivative of the phase term simply yields the phase difference over the junction, i.e. eq. (A.2) can be written as:

$$\varphi(y) = \int_{-d/2}^{d/2} \frac{2\pi}{\Phi_0} A_x(x, y) dx + \gamma\left(\frac{d}{2}, y\right) - \gamma\left(-\frac{d}{2}, y\right) \quad (\text{A.3})$$

We proceed by integrating $\nabla\gamma$ over the rectangular loop of Figure A.1, assuming that the current-phase relation is dominated by the first harmonic – which is true if the electrodes are weakly coupled – such that we can set $n = 0$ in $\oint_C \nabla\gamma d\ell = 2\pi n$. We also rewrite the second Ginzburg-Landau equation to the form $\nabla\gamma = -\frac{2\pi\mu_0\lambda_L^2}{\Phi_0}\mathbf{J} - \frac{2\pi}{\Phi_0}\mathbf{A}$ and substitute the result in the integrals over C_2 and C_4 to obtain:

$$\begin{aligned}
0 &= \oint_C \nabla \gamma d\ell \\
&= \int_{-d/2}^{d/2} \frac{\partial}{\partial x} \gamma(x, 0) dx + \int_{-d/2}^{d/2} \frac{\partial}{\partial x} \gamma(x, y) dx \\
&\quad + \int_0^y \left(\frac{-2\pi}{\Phi_0} A_y \left(\frac{d}{2}, y' \right) - \frac{2\pi\mu_0\lambda_L^2}{\Phi_0} J_y \left(\frac{d}{2}, y' \right) \right) dy' \\
&\quad + \int_y^0 \left(\frac{-2\pi}{\Phi_0} A_y \left(-\frac{d}{2}, y' \right) - \frac{2\pi\mu_0\lambda_L^2}{\Phi_0} J_y \left(-\frac{d}{2}, y' \right) \right) dy' \\
&= \left(\gamma \left(\frac{d}{2}, 0 \right) - \gamma \left(-\frac{d}{2}, 0 \right) \right) + \left(\gamma \left(-\frac{d}{2}, y \right) - \gamma \left(\frac{d}{2}, y \right) \right) + \dots
\end{aligned}$$

We can use eq. (A.3) to write the expression involving γ in terms of the gauge-invariant phase difference φ and the x-component of the vector potential A_x :

$$0 = \left(-\varphi(0) - \frac{2\pi}{\Phi_0} \int_{-d/2}^{d/2} A_x(x, 0) dx \right) + \left(\varphi(y) + \frac{2\pi}{\Phi_0} \int_{-d/2}^{d/2} A_x(x, y) dx \right) + \dots$$

Multiplying the equation by -1 and grouping terms yields:

$$\begin{aligned}
0 &= \varphi(0) - \varphi(y) + \frac{2\pi}{\Phi_0} \int_{-d/2}^{d/2} A_x(x, 0) dx - \frac{2\pi}{\Phi_0} \int_{-d/2}^{d/2} A_x(x, y) dx \\
&\quad + \frac{2\pi}{\Phi_0} \int_0^y A_y \left(\frac{d}{2}, y' \right) dy' + \frac{2\pi}{\Phi_0} \int_y^0 A_y \left(-\frac{d}{2}, y' \right) dy' \\
&\quad + \frac{2\pi\mu_0\lambda_L^2}{\Phi_0} \left(\int_0^y J_y \left(\frac{d}{2}, y' \right) dy' + \int_y^0 J_y \left(-\frac{d}{2}, y' \right) dy' \right) \\
&= \varphi(0) - \varphi(y) + \frac{2\pi}{\Phi_0} \oint_C \mathbf{A} d\ell + \frac{2\pi\mu_0\lambda_L^2}{\Phi_0} \left(\int_0^y J_{y,R} \left(\frac{d}{2}, y' \right) dy' + \int_y^0 J_{y,L} \left(-\frac{d}{2}, y' \right) dy' \right)
\end{aligned} \tag{A.4}$$

Which is eq. (2.27) in [8]. Note that by reasons of symmetry $J_{y,R} \left(\frac{d}{2}, y' \right) = -J_{y,L} \left(-\frac{d}{2}, y' \right)$. Next, we rewrite the line integral over the vector potential using Stokes' theorem:

$$\oint_C \mathbf{A} d\ell = \iint_{\Sigma} \nabla \times \mathbf{A} d\mathbf{S} = \iint_{\Sigma} \mathbf{B} d\mathbf{S} = \Phi = Byd \tag{A.5}$$

where Φ is the magnetic flux through the loop and Σ is the surface enclosed by the loop. Using these results, we arrive at eq. (2.28) in [8], which corresponds to eq. (5) in [3]:

$$\varphi(y) = \varphi(0) + \frac{2\pi}{\Phi_0} \left(Byd + 2\mu_0\lambda_L^2 \int_0^y J_{y,R}\left(\frac{d}{2}, y'\right) dy' \right) \quad (\text{A.6})$$

The integral over $J_{y,R}\left(\frac{d}{2}, y\right)$ can be evaluated by rewriting it in terms of phase and vector potential from the second Ginzburg-Landau equation and realizing that $A_y = 0$, by design:

$$\begin{aligned} 2\mu_0\lambda_L^2 \int_0^y J_{y,R}\left(\frac{d}{2}, y'\right) dy' &= 2\mu_0\lambda_L^2 \int_0^y -\frac{\Phi_0}{2\pi\mu_0\lambda_L^2} \frac{\partial}{\partial y} \gamma\left(\frac{d}{2}, y'\right) dy' \\ &= -\frac{\Phi_0}{\pi} \left[\gamma\left(\frac{d}{2}, y\right) - \gamma\left(\frac{d}{2}, 0\right) \right] = -\frac{\Phi_0}{\pi} \gamma\left(\frac{d}{2}, y\right) \end{aligned} \quad (\text{A.7})$$

Inserting the result in eq. (A.6), we obtain the phase difference over the junction:

$$\varphi(y) = \varphi(0) + \frac{2\pi}{\Phi_0} Byd - 2\gamma\left(\frac{d}{2}, y\right) \quad (\text{A.8})$$

Integrating the first Josephson relation $J_x = J_c \sin \varphi(y)$ over the surface enclosed by the loop gives the current across the junction:

$$\begin{aligned} I(B) &= \iint_{\Sigma} \mathbf{J} d\mathbf{S} \\ &= \int_{-W/2}^{W/2} t_{junc} J_c \sin \left(\varphi(0) + \frac{2\pi}{\Phi_0} Byd - 2\gamma\left(\frac{d}{2}, y\right) \right) dy \end{aligned} \quad (\text{A.9})$$

where t_{junc} is the thickness of the junction and W the width in the y -direction. Next, we assume a uniform zero-field critical current density over the junction such that $J_c = I_c(0) \setminus t_{junc} W$. The critical current is reached if the junction is phase-biased by $\pi \setminus 2$, that is, if we set $\varphi(0) = \pi \setminus 2$.

$$\frac{I_c(B)}{I_c(0)} = \frac{1}{W} \left| \int_{-W/2}^{W/2} \cos \left(\frac{2\pi}{\Phi_0} Byd - 2\gamma\left(\frac{d}{2}, y\right) \right) dy \right| \quad (\text{A.10})$$

Eq. (A.20) is eq. (12) in [3]; it can be solved numerically by iterating over an array of B -values for the applied magnetic field. For computational reasons we assume that the phase-terms γ , which have a B -dependency via the boundary conditions imposed on the Laplace equation, scale linearly with B . This simplification eliminates the need to evaluate $\gamma(-\frac{d}{2}, y)$ and $\gamma(\frac{d}{2}, y)$ for every iteration and was found

to yield good results in [3]. Furthermore, we assume $2\pi Byd/\Phi_0 \sim 0$ because d is very small. Eq. (A.10) then changes to:

$$\frac{I_c(B)}{I_c(0)} = \frac{1}{W} \left| \int_{-W/2}^{W/2} \cos \left(2B\gamma \left(\frac{d}{2}, y \right) \right) dy \right| \quad (\text{A.11})$$

which is eq. (3.2).

A.1.1 Note on macroscopic junctions

For macroscopic junctions, we have

$$J_y \left(\frac{d}{2}, y \right) = \frac{B}{\mu_0 \lambda_L} \quad (\text{A.12})$$

which follows directly from eq. (2.5) for $x = 0$. From this we see that eq. (A.6) takes on the simpler form:

$$\varphi(y) = \varphi(0) + \frac{2\pi}{\Phi_0} (Byd + 2By\lambda_L) = \varphi_0 + \frac{2\pi(2\lambda_L + d)B}{\Phi_0} y \quad (\text{A.13})$$

We can define the *effective junction length* $L_{eff} = 2\lambda_L + d$. Integrating the first Josephson relation in the same way we did before, we obtain the result:

$$I(B) = \int \mathbf{J} d\mathbf{S} = \int_{-W/2}^{W/2} t_{junc} J_c \sin \left(\varphi(0) + \frac{2\pi L_{eff} B}{\Phi_0} y \right) dy \quad (\text{A.14})$$

where t_{junc} is the thickness of the junction. If we, furthermore, assume that the critical current at zero field is equally distributed over the cross-section of the junction (i.e. $J_c = I_c(0)/t_{junc}W$) and if we current-bias the junction by $\pi/2$, the expression for the critical current as a function of magnetic field becomes:

$$\begin{aligned} \frac{I_c(B)}{I_c(0)} &= \left| \frac{1}{W} \int_{-W/2}^{W/2} \cos \left(\frac{2\pi L_{eff} B}{\Phi_0} y \right) dy \right| = \left| \frac{\sin \left(\frac{\pi L_{eff} WB}{\Phi_0} \right)}{\frac{\pi L_{eff} WB}{\Phi_0}} \right| \\ &= \left| \frac{\sin \left(\frac{\pi \Phi}{\Phi_0} \right)}{\frac{\pi \Phi}{\Phi_0}} \right| = \left| \text{sinc} \left(\frac{\pi \Phi}{\Phi_0} \right) \right| \quad (\text{A.15}) \end{aligned}$$

In eq. (A.15), we recognize the expression for the classic Fraunhofer pattern.

A.2 Brief note on modifying the formalism to allow non-identical electrodes

To generalize the formalism in order to include junctions in which the two electrodes do not have the same shape – i.e. the junction is asymmetric in the y -axis (but still symmetric with respect to the x -axis) – consider that it is no longer possible to assume that the current density on both sides of the junction is symmetrically distributed; in general, it holds that $J_{y,R}(\frac{d}{2}, y) \neq -J_{y,L}(-\frac{d}{2}, y)$. As a consequence, we cannot rearrange the integrals as was done in equation (A.6).

$$\varphi(y) = \varphi(0) + \frac{2\pi}{\Phi_0} \left(Byd + \mu_0 \lambda_L^2 \left[\int_0^y J_{y,R}\left(\frac{d}{2}, y'\right) dy' + \int_y^0 J_{y,L}\left(-\frac{d}{2}, y'\right) dy' \right] \right) \quad (\text{A.16})$$

Instead, we find that

$$\begin{aligned} \mu_0 \lambda_L^2 \int_0^y J_{y,R}\left(\frac{d}{2}, y'\right) dy' &= \mu_0 \lambda_L^2 \int_0^y -\frac{\Phi_0}{2\pi\mu_0\lambda_L^2} \frac{\partial}{\partial y} \gamma\left(\frac{d}{2}, y'\right) dy' \\ &= -\frac{\Phi_0}{2\pi} \left[\gamma\left(\frac{d}{2}, y\right) - \gamma\left(\frac{d}{2}, 0\right) \right] = -\frac{\Phi_0}{2\pi} \gamma\left(\frac{d}{2}, y\right) \end{aligned} \quad (\text{A.17})$$

$\gamma(\frac{d}{2}, 0) = 0$ follows from symmetry in the x -axis (the phase on the line $y = 0$ should vanish because this is the internal axis of symmetry for each of the electrodes). Likewise,

$$\begin{aligned} \mu_0 \lambda_L^2 \int_y^0 J_{y,L}\left(-\frac{d}{2}, y'\right) dy' &= \mu_0 \lambda_L^2 \int_y^0 -\frac{\Phi_0}{2\pi\mu_0\lambda_L^2} \frac{\partial}{\partial y} \gamma\left(-\frac{d}{2}, y'\right) dy' \\ &= \frac{\Phi_0}{2\pi} \gamma\left(-\frac{d}{2}, y\right) \end{aligned} \quad (\text{A.18})$$

So we can write:

$$\varphi(y) = \varphi(0) + \frac{2\pi}{\Phi_0} Byd + \left[\gamma\left(-\frac{d}{2}, y\right) - \gamma\left(\frac{d}{2}, y\right) \right] \quad (\text{A.19})$$

Following the steps from the symmetrical treatment, we find that:

$$\frac{I_c(B)}{I_c(0)} = \frac{1}{W} \left| \int_{-W/2}^{W/2} \cos \left(\frac{2\pi}{\Phi_0} Byd + \gamma\left(-\frac{d}{2}, y\right) - \gamma\left(\frac{d}{2}, y\right) \right) dy \right| \quad (\text{A.20})$$

Using the same logic, eq. (A.20) can be cast into the computationally more efficient form:

$$\frac{I_c(B)}{I_c(0)} = \frac{1}{W} \left| \int_{-W/2}^{W/2} \cos \left(B \left[\gamma\left(-\frac{d}{2}, y\right) - \gamma\left(\frac{d}{2}, y\right) \right] \right) dy \right| \quad (\text{A.21})$$

Mathematical background of the Hausdorff and box dimension

In Section 2.4, we encountered the problem of conceptualizing a more rigorous measure of ‘detail’ in the context of scaling fractal geometries. To resolve this, we make the notion of dimensionality more precise by defining the Hausdorff dimension. Before this, we make explicit the concept of an *open ball*. Having done this, we bridge the gap between the Hausdorff and box dimension by establishing their equivalency with Proposition B.0.1.

Definition B.0.1 (Open ball). The *open ball* $B(p, r)$ of radius r centred on the point p in Euclidean space is the set

$$B(p, r) = \{x : \text{dist}(x, p) < r\}$$

where $\text{dist}(x, p)$ is the distance between points x and p .

Definition B.0.2 (Hausdorff dimension). Let X be the subset of an Euclidean space. For each $r > 0$, let $N(r)$ denote the smallest number of open balls of radius r needed to cover X . The limit

$$D = \lim_{r \rightarrow 0} (-\log N(r) / \log r)$$

can be shown to exist and the value of D is called the Hausdorff dimension of X .

Proposition B.0.1. Let X be a set of Hausdorff dimension D embedded in Euclidean space. Then the box dimension of X is also D .

Acknowledgements

Looking back on the proceedings of the past four months, I want to extend my sincere gratitude to Remko Fermin and Kaveh Lahabi in particular for their commitment and their unrelenting support to this project, even though the odds of making strides forward did not look equally bright at all times. On a similar note, I will not forget the scientific enthusiasm encountered in our shared group meetings, interspersed with the copious amounts of humour and optimism exhibited by everybody affiliated to the Lahabi and Semonti lab. Many thanks also to Wolfgang Löffler, for agreeing to assess my work without hesitation. Joining all of you for this brief time taught me more than a year of any courses could have accomplished.

Bibliography

- [1] S. N. Kempkes, M. R. Slot, S. E. Freeney, S. J. Zevenhuizen, D. Vanmaekelbergh, I. Swart, and C. M. Smith, *Design and characterization of electrons in a fractal geometry*, Nature physics **15**, 127 (2019).
- [2] J. R. Clem, *Josephson junctions in thin and narrow rectangular superconducting strips*, 2010, PRB.
- [3] R. Fermin, B. de Wit, and J. Aarts, *Beyond the effective length: How to analyze magnetic interference patterns of thin-film planar Josephson junctions with finite lateral dimensions*, Physical Review B **107**, 064502 (2023).
- [4] J. F. Annett, *Superconductivity, superfluids and condensates*, volume 5, Oxford University Press, 2004.
- [5] M. Tinkham, *Introduction to Superconductivity: Second Edition*, Dover Publications, 2004.
- [6] H. Hastings and G. Sugihara, *Fractals: A User's Guide for the Natural Sciences*, Oxford University Press, 1993.
- [7] V. Moshchalkov and J. Fritzsch, *Nanostructured superconductors*, World Scientific, 2011.
- [8] R. Fermin, *Size effects in microstructured superconductors and quantum materials*, Thesis, Leiden University, 2022.
- [9] H. Kleinert, *Disorder version of the Abelian Higgs model and the order of the superconductive phase transition*, Lettere al Nuovo Cimento (1971-1985) **35**, 405 (1982).
- [10] J. Hove, S. Mo, and A. Sudbø, *Vortex interactions and thermally induced crossover*

- from type-I to type-II superconductivity*, Physical Review B **66**, 064524 (2002), PRB.
- [11] L. Xu, Z. Shu, and S. Wang, *From BCS theory for isotropic homogeneous systems to the complete Ginzburg-Landau equations for anisotropic inhomogeneous systems*, Physical Review B **57**, 11654 (1998).
 - [12] S. Nettel, *Relationship between Ginzburg-Landau and BCS theory*, Physical Review B **48**, 13709 (1993).
 - [13] S. J. Chapman and D. R. Heron, *A Hierarchy of Models for Superconducting Thin Films*, SIAM Journal on Applied Mathematics **63**, 2087 (2003).
 - [14] J. Pearl, *Current distribution in superconducting films carrying quantized fluxoids*, Applied Physics Letters **5**, 65 (1964).
 - [15] M. Zgirski, K.-P. Riikonen, V. Touboltsev, and K. Arutyunov, *Size Dependent Breakdown of Superconductivity in Ultranarrow Nanowires*, Nano Letters **5**, 1029 (2005).
 - [16] K. Y. Arutyunov, D. S. Golubev, and A. D. Zaikin, *Superconductivity in one dimension*, Physics Reports **464**, 1 (2008).
 - [17] C. N. Lau, N. Markovic, M. Bockrath, A. Bezryadin, and M. Tinkham, *Quantum Phase Slips in Superconducting Nanowires*, Physical Review Letters **87**, 217003 (2001), PRL.
 - [18] F. Altomare and A. Chang, *One-Dimensional Superconductivity in Nanowires*, Wiley, 2013.
 - [19] N. Markovic, C. N. Lau, and M. Tinkham, *The limits of superconductivity in MoGe nanowires*, Physica C: Superconductivity **387**, 44 (2003).
 - [20] A. Bezryadin, *Quantum suppression of superconductivity in nanowires*, Journal of Physics: Condensed Matter **20**, 043202 (2008).
 - [21] Y. Takahide, H. Miyazaki, A. Kanda, and Y. Ootuka, *Dimensional crossover from 2D to 1D in small-Josephson-junction arrays*, Physica B: Condensed Matter **329**, 1407 (2003).
 - [22] Y. Takahide, H. Miyazaki, and Y. Ootuka, *Superconductor-insulator crossover in Josephson junction arrays due to reduction from two to one dimension*, Physical Review B **73**, 224503 (2006).
 - [23] R. Meyer, S. Korshunov, C. Leemann, and P. Martinoli, *Dimensional crossover*

- and hidden incommensurability in Josephson junction arrays of periodically repeated Sierpinski gaskets,* Physical Review B **66**, 104503 (2002).
- [24] P. W. Anderson, *Theory of dirty superconductors*, Journal of Physics and Chemistry of Solids **11**, 26 (1959).
 - [25] S. Vlaic, S. Pons, T. Zhang, A. Assouline, A. Zimmers, C. David, G. Rodary, J.-C. Girard, D. Roditchev, and H. Aubin, *Superconducting parity effect across the Anderson limit*, Nature Communications **8**, 14549 (2017).
 - [26] M. Shishikura, *The Hausdorff dimension of the boundary of the Mandelbrot set and Julia sets*, Annals of Mathematics , 225 (1998).
 - [27] Prokofiev, *Great Britain Box*, https://commons.wikimedia.org/wiki/File:Great_Britain_Box.svg#filelinks, 2010, Accessed: 10-06-2023.
 - [28] W. Rasband, *ImageJ*, <https://imagej.nih.gov/ij/>, 1997-2018, Accessed: 10-06-2023.
 - [29] A. Karperien, *FracLac for ImageJ*, <http://rsb.info.nih.gov/ij/plugins/fraclac/FLHelp/Introduction.htm>, 1999-2013, Accessed: 10-06-2023.
 - [30] R. Dynes and T. Fulton, *Supercurrent density distribution in Josephson junctions*, Physical Review B **3**, 3015 (1971).
 - [31] S. Mandal, S. Dutta, S. Basistha, I. Roy, J. Jesudasan, V. Bagwe, L. Benfatto, A. Thamizhavel, and P. Raychaudhuri, *Destruction of superconductivity through phase fluctuations in ultrathin a-MoGe films*, Physical Review B **102**, 060501 (2020).
 - [32] C. Poole, H. Farach, and R. Creswick, *Handbook of Superconductivity*, Elsevier Science, 1999.
 - [33] A. A. Boris, A. Rydh, T. Golod, H. Motzkau, A. Klushin, and V. M. Krasnov, *Evidence for nonlocal electrodynamics in planar Josephson junctions*, Physical Review Letters **111**, 117002 (2013).
 - [34] A. Franz, A. Wallraff, and A. V. Ustinov, *Magnetic field penetration in a long Josephson junction imbedded in a wide stripline*, Journal of Applied Physics **89**, 471 (2001).
 - [35] G. J. C. van Baarle, *Vortices in superconductors imaged by Scanning Tunnelling Microscopy: vortex structures in superconducting thin films of a-Mo₂.7Ge and (La, Sr) 2 CuO₄*, Thesis, Leiden University, 2005.
-

- [36] J. M. Gordon, A. M. Goldman, J. Maps, D. Costello, R. Tiberio, and B. Whitehead, *Superconducting-normal phase boundary of a fractal network in a magnetic field*, Physical review letters **56**, 2280 (1986).
- [37] R. Rammal and G. Toulouse, *Spectrum of the Schrödinger equation on a self-similar structure*, Physical review letters **49**, 1194 (1982).
- [38] J. Villegas, S. Savel'ev, F. Nori, E. Gonzalez, J. Anguita, R. Garcia, and J. Vicent, *A superconducting reversible rectifier that controls the motion of magnetic flux quanta*, science **302**, 1188 (2003).
- [39] J. I. Martin, M. Vélez, J. Nogués, and I. K. Schuller, *Flux pinning in a superconductor by an array of submicrometer magnetic dots*, Physical review letters **79**, 1929 (1997).
- [40] J. Villegas, M. Montero, C.-P. Li, and I. K. Schuller, *Correlation length of quasiperiodic vortex lattices*, Physical review letters **97**, 027002 (2006).
- [41] M. Vélez, J. Martín, J. Villegas, A. Hoffmann, E. Gonzalez, J. Vicent, and I. K. Schuller, *Superconducting vortex pinning with artificial magnetic nanostructures*, Journal of Magnetism and Magnetic Materials **320**, 2547 (2008).
- [42] C. C. de Souza Silva, J. Van de Vondel, B. Zhu, M. Morelle, and V. Moshchalkov, *Vortex ratchet effects in films with a periodic array of antidots*, Physical Review B **73**, 014507 (2006).
- [43] J. Van de Vondel, C. de Souza Silva, B. Zhu, M. Morelle, and V. Moshchalkov, *Vortex-rectification effects in films with periodic asymmetric pinning*, Physical review letters **94**, 057003 (2005).
- [44] S. Benz, M. Rzchowski, M. Tinkham, and C. Lobb, *Fractional giant Shapiro steps and spatially correlated phase motion in 2D Josephson arrays*, Physical review letters **64**, 693 (1990).
- [45] K. Lee, D. Stroud, and J. Chung, *Calculation of giant fractional Shapiro steps in Josephson-junction arrays*, Physical review letters **64**, 962 (1990).
- [46] J. Free, S. Benz, M. Rzchowski, M. Tinkham, C. Lobb, and M. Octavio, *Dynamical simulations of fractional giant Shapiro steps in two-dimensional Josephson arrays*, Physical Review B **41**, 7267 (1990).
- [47] R. Panghotra, B. Raes, C. C. de Souza Silva, I. Cools, W. Keijers, J. Scheerder, V. Moshchalkov, and J. Van de Vondel, *Giant fractional Shapiro steps in anisotropic Josephson junction arrays*, Communications Physics **3**, 53 (2020).